Ocean Engineering 300 (2024) 117498

Contents lists available at ScienceDirect

Ocean Engineering

journal homepage: www.elsevier.com/locate/oceaneng

Research paper

Numerical analysis of aero-hydrodynamic wake flows of a floating offshore wind turbine subjected to atmospheric turbulence inflows

Shun Xu [a], Xiaolong Yang [b], Weiwen Zhao [a], Decheng Wan [a,*]

[a] Computational Marine Hydrodynamics Lab (CMHL), School of Naval Architecture, Ocean and Civil Engineering, Shanghai Jiao Tong University, Shanghai, China
[b] Offshore Oil Engineering Co. Ltd., Tianjin, China

ARTICLE INFO

Keywords:
Atmospheric inflow
Floating offshore wind turbine
Aero-hydrodynamics
Wake characteristics

ABSTRACT

The influence of atmospheric turbulence inflow on coupled dynamic behaviors and wakes of floating offshore wind turbine (FOWT) is pronounced, especially as blade size increases. In this study, we explore the effects of atmospheric inflow on aero-hydrodynamics and wake characteristics of a spar-type FOWT. A well-validated in-house computational fluid dynamic (CFD) solver, FOWT-UALM-SJTU, is utilized to conduct the numerical simulations. To generate the realistic atmospheric inflow condition, the large eddy simulation (LES) with long-duration is employed. Two other cases involving uniform inflow and shear inflow are conducted to provide some comparable results. Compared to uniform inflow and shear inflow, the power and thrust of FOWT under atmospheric inflow display greater instability, with their power spectrums exhibiting higher intensity in high frequency region. The variation of yaw moment in atmospheric scenario is significantly drastic, leading to a remarkable response in platform yaw motion. Notably, the dominant frequency in this scenario is the blade passage frequency, as opposed to the incident wave frequency observed in the uniform and shear scenarios. The atmospheric inflow promotes the manifestation of wake breakdown and wake meandering, resulting in the faster wake recovery of FOWT. Besides, the meandering in the far wake is more significant compared to uniform and shear scenarios. The absence of vortex rings in atmospheric scenario is observed, along with the presence of more complex and smaller vortices in far wake. Our findings highlight the remarkable impacts of atmospheric inflow on dynamic responses and wake evolution of FOWT, and it is recommended that the atmospheric inflow be taken into account when assessing wake interactions between multiple FOWTs.

1. Introduction

The floating offshore wind turbine (FOWT) is a feasible solution for harvesting the rich and high-quality wind resources in deep sea (Xu et al., 2022). With the development of offshore wind energy, the design and construction of FOWT has become an attractive topic. The FOWT is a highly integrated system composed of wind turbine, floating platform and mooring system. Due the combined wind-wave-current conditions, the aero-hydrodynamics of FOWT exhibit remarkable coupling characteristics (Tran and Kim, 2016; Huang et al., 2023a). To support the design of FOWT and guarantee its safe operation, the accurate prediction of the dynamic behaviors of FOWT is a critical thing. Three research methods are usually employed, the prototype, scale-down experiment and numerical simulation (Otter et al., 2022; Chen et al., 2020). Among those research methods, the cost of numerical simulation of FOWT is cheapest and has received increasing attention with the help of high-performance computer.

Considering the complex coupled aero-hydrodynamics of FOWT, many researchers simplified the platform motion to a prescribed motion to investigate the unsteady aerodynamics of wind turbine. In terms of six-degree-of-freedom (6DoF) motions of floating platform, the prescribed surge motion and pitch motion are suggested due to their significant effects on angle of attack of turbine blades. Mancini et al. (2020) studied the unsteady aerodynamic responses of FOWT under pitch motion. The results from different numerical models were firstly validated against experiments, and subsequently, they conducted a conclusion that the unsteady responses were dominated by first surge harmonic. Dong and Viré (2022) investigated the aerodynamics of FOWT experiencing various working states in a full cycle of pitch motion. The vortex ring state is demonstrated to be the most unstable by evaluating the aerodynamic load. Huang and Wan (2019) pointed out that the impacts of pitch motion on relative wind speed of blades were more pronounced

* Corresponding author.
E-mail address: dcwan@sjtu.edu.cn (D. Wan).

https://doi.org/10.1016/j.oceaneng.2024.117498
Received 23 December 2023; Received in revised form 10 March 2024; Accepted 11 March 2024

compared to surge motion, although the both could alter the local angle of attack. What's more, they observed the wake deflection in near wake when considering pitch motion. Through their study of the aerodynamics and wakes of FOWT in presence of pitch motion, Fu et al. (2023) highlighted that the pitch motion significantly affects power, thrust and wake characteristics of wind turbine.

In addition to the individual 6DoF motion, some researches have also considered multiple platform motions and studied their effects on wind turbine aerodynamics and wakes, which represent a more realistic scenario. Chen et al. (2021) importantly noted that the power of FOWT is reduced with combined surge-pitch motion, reflecting the negative effects of sophisticated platform motions on power generation of FOWT. Lee and Lee (2019) investigated the wakes of FOWT with different supporting platforms and multiple platform motions. Their findings revealed the strong effects of platform motions on wake evolution, and thus resulting in the quick breakdown of wake vortices. Arabgolarcheh et al. (2023) analyzed the middle-to-far wake of FOWT considering multiple platform motions. It was found that the rotational motions of platform can induce non-axisymmetric helical wake and benefit the wake meandering.

Although the prescribed platform motions present the interesting and valuable results for unsteady aerodynamics and wakes, the strong interference between wind turbine and floating platform is not considered. It is necessary to take into account the fully coupled aero-hydrodynamics because the FOWT is subjected to combined wind-wave loads. Zhang and Kim (2018) performed the aero-hydrodynamic analysis for a semi-submersible FOWT. They found that, in comparison to onshore wind turbine, the FOWT exhibited a 7.8% increase in thrust but a 10% decrease in power. Building upon the coupled aero-hydrodynamics of FOWT, Feng et al. (2023) also incorporated the pitch motion of blade into their analysis. Their findings revealed that the pitch motion of blade resulted in a decrease in aerodynamic loads while amplifying the response amplitude of the platform. In order to reduce the computational cost in simulations of FOWT, Cheng et al. (2019) proposed a solver called FOWT-UALM-SJTU, which combines the actuator line model (ALM) with their in-house two-phase computational fluid dynamics (CFD) solver, naoe-FOAM-SJTU. The latter was originally developed for hydrodynamics of marine structures in various sea states. The unsteady aerodynamics of FOWT were implemented by incorporating an additional velocity resulting from platform motions into the conventional ALM. The ability of FOWT-UALM-SJTU for predicting aero-hydrodynamic responses of FOWT was comprehensively validated. Subsequently, Huang et al. (2023b) employed the FOWT-UALM-SJTU solver to explore the wake interaction between two FOWTs. Various layouts, including tandem and offset configurations, were examined, and a detailed analysis of the dynamic responses and wake characteristics of FOWTs was conducted.

The previous studies related to numerical investigations of FOWT did not consider the complex atmospheric boundary layer (ABL) inflow (Johlas et al., 2019, 2020), instead, they relied on uniform or shear inflows. When utilizing the atmospheric inflow, some conclusions drawn from simplified inflows may change. The results from Kleine et al. (2022) presented the large flow structures in wind turbine wakes with different motion modes, even as far downstream as six diameters from the wind turbine. However, they emphasized the need for cautious consideration of this conclusion when transitioning the inflow wind from uniform inflow to atmospheric inflow, as these flow structures can be modified and dissipated by free-stream turbulence. With the increasing size of wind turbine to harvest more wind energy and decrease operation costs, the influence of atmospheric turbulence inflow on its aerodynamic performance and wake characteristics becomes increasingly significant (Porté-Agel et al., 2020; Lu and Porté-Agel, 2011; Hansen et al., 2012; Abkar and Porté-Agel, 2015). Li et al. (2018) investigated the effects of atmospheric inflows on aerodynamic performance of a FOWT, conducting that the power generation of FOWT is highly sensitive to atmospheric turbulence inflow. Similarly, Xu et al. (2023a) highlighted that the power variation of a semi-submersible FOWT was primarily determined by turbulence in atmospheric inflow, rather than the platform motions. In addition to studying dynamic responses, Zhou et al. (2022) also explored the impacts of inflow wind condition on wake characteristics of FOWT. Their results revealed that a quicker wake diffusion was observed in atmospheric scenario compared to time-independent inflow wind. However, due to the limitation of expensive computational costs, the difference of wake evolution in far wake under different wind inflows conditions was not presented.

In this study, a numerical study on the effects of atmospheric inflow on aero-hydrodynamics and wake characteristics of FOWT is conducted. The well-validated in-house CFD solver, FOWT-UALM-SJTU, is utilized to predict the coupled aero-hydrodynamics and wakes of FOWT. This solver employs the ALM incorporated with an additional velocity from platform motions to capture unsteady aerodynamics of FOWT. In comparison to blade-resolved method, this approach reduces the burden of expensive computational costs, allowing us to investigate the wake evolution in far wake. What's more, the wake interaction between muti-FOWTs can also be studied with acceptable computational cost, which is very helpful for the power prediction of a large floating wind farm. We employ the large eddy simulation (LES) with long-duration simulation to generate the atmospheric inflow condition. Two additional wind inflows, uniform inflow and shear inflow, are used to provide some comparable results. The results in aerodynamic performance, platform motions, as well as wake characteristics are compared and analyzed in detail.

The remainder of this study is organized as follows. In Section 2, the numerical methods involve governing equations, modeling of aerodynamics, hydrodynamics and mooring system, as well as generation of atmospheric inflow are presented. Validations of simulated atmospheric inflow and wake modeling are exhibited in Section 3. Section 4 shows the simulation details, including the FOWT model and computational setup. In Section 5, the mesh convergence study is conducted, subsequently, the results in aerodynamics, hydrodynamics and wakes among three wind conditions are compared and analyzed. Some conclusions are drawn in Section 6.

2. Numerical methods

2.1. Governing equations

Three-dimensional Navier-Stokes equations are used to simulate the fully coupled aero-hydrodynamics and wakes of FOWT, in which the fluid is considered to be viscous and incompressible. The continuity and momentum equations are as follows:

$$\nabla \bullet U = 0 \tag{1}$$

$$\frac{\partial(\rho U)}{\partial t} + \nabla \bullet (\rho UU) = -\nabla p_d - g \bullet x \nabla \rho + \nabla \bullet \left(\mu_{eff} \nabla \mathrm{U}\right) + f_\sigma + f_s + f_\varepsilon \tag{2}$$

where, U is velocity of flow fluid; ρ denotes density of two-phase fluid; $p_d = p - \rho g x$ is dynamic pressure by subtracting the static pressure from total pressure; g is gravity acceleration; x is Cartesian coordinate vector; $\mu_{eff} = \mu + \mu_t$ is effective viscosity, where μ and μ_t are molecular and eddy viscosities, respectively; f_σ denotes a source term of tension force of free surface, which is active only near the air-water interface; f_s is a source term of wave absorption and active in domain of wave absorption; f_ε is a source term of body force of wind turbine aerodynamic loads, which can be determined by ALM.

The Reynolds-averaged Navier–Stokes (RANS) model is a common practice for fully coupled aero-hydrodynamics of FOWT. However, the far wake evolution of FOWT is also an interest in the present study. Consequently, the Delayed Detached Eddy Simulation (DDES) method (Spalart et al., 2006) is utilized to closure the above momentum equation. The DDES model combines the advantages of RANS and LES. This

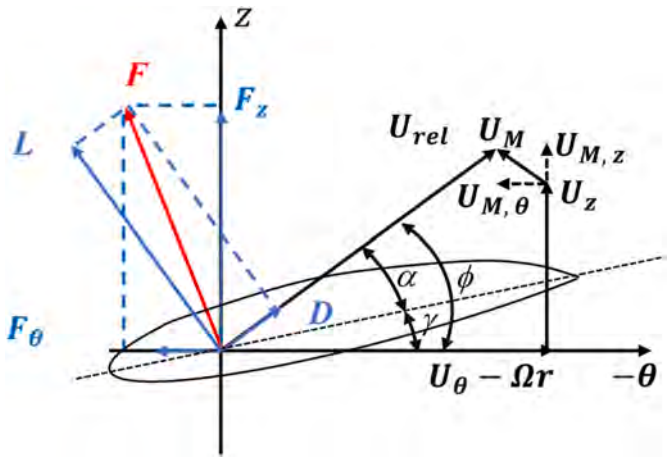

Fig. 1. Velocity vectors at a blade section.

mode reduces the requirement for mesh resolution near the wall and also guarantee the numerical accuracy in the wake region (Chen et al., 2022). Compared to the conventional DES model, a shielding function is introduced into the DDES model to avoid the early switch to the LES mode within boundary layer. More descriptions of this DDES model can refer to this literature (Spalart et al., 2006).

The current simulations are performed using the finite volume method (FVM). The temporal term is discretized with Euler scheme. The convective and diffusive terms are discretized with second order upwind and central differencing schemes, respectively. The PIMPLE algorithm, a hybrid of PISO and SIMPLE, is implemented to handle the pressure-velocity coupling, utilizing three outer-corrector loops and two inner-corrector loops.

2.2. Aerodynamic modeling

The wind turbine aerodynamics are modeled and simulated by the ALM. Compared to high-fidelity blade-resolved method, the computational cost is affordable without resolving the boundary layer of blade surface and numerical accuracy is guaranteed by resolving Navier-Stokes governing equations of flow field (Troldborg et al., 2007). Consequently, the ALM has been widely used in numerical studies of wind turbine, especially for far wakes (Wang et al., 2023; Li et al., 2022). The idea behind ALM is to represent the wind turbine blades by virtual lines with a series of actuator points distributed radially. The aerodynamic forces of actuator points are calculated based on the blade element theory, in which the relative wind speed and angle of attack at blade section are required. Then the aerodynamic forces of actuator points are projected into flow field to reflect the effect of wind turbine on flow field, and a smooth function is suggested in this process to avoid the numerical singularity in simulation procedure.

Compared to the conventional ALM, an additional wind speed induced by platform motions is considered and employed for aerodynamics of FOWT. Fig. 1 shows the velocity vectors at a blade section. The relative wind speed U_{rel} at the blade section is determined by:

$$U_{rel} = U_\theta - \Omega r + U_z + U_M \tag{3}$$

where, U_θ, U_z are the tangential and axial components of inflow wind speed; Ω is the rotor speed of wind turbine; r is the radius from blade section to rotor center; U_M is the additional wind speed induced by platform motions.

The angle of attack α is calculated by:

$$\alpha = \varphi - \beta \tag{4}$$

where, φ is the inflow angle at blade section; β is the pitch angle of blade. According to the velocity vectors in Fig. 1, the inflow angle φ is expressed as:

$$\varphi = tan^{-1}\left(\frac{U_z + U_{M,z}}{\Omega r + U_{M,\theta} - U_\theta}\right) \tag{5}$$

where, $U_{M,\theta}$, $U_{M,z}$ are tangential and axial components of additional wind speed, respectively. Once the relative wind speed U_{rel} and angle of attack α are obtained, the aerodynamic forces of actuator points can be expressed by:

$$f = (L, D) = \frac{1}{2}\rho U_{rel}^2 c dr (C_L \vec{} e_L + C_D \vec{} e_D) \tag{6}$$

where, ρ is the air density; c is the chord length; dr is the width of blade section; C_L, C_D are the coefficients of lift and drag, which are determined by attack of angle α; $\vec{e_L}$, $\vec{e_D}$ are the unit vectors of lift and drag, respectively.

By integrating the aerodynamic forces of all blade sections of blades, the aerodynamic loads (i.e., rotor thrust, rotor torque) are obtained. As aforementioned, the aerodynamic forces of actuator points need to be projected into flow field to represent the effect of wind turbine on flow field and reproduce wind turbine wakes. To avoid the numerical singularity, the aerodynamic forces need to be smoothed in this projection process and the Gauss kernel function is used. The aerodynamic forces of actuator points after smoothing are introduced into momentum equation as a source term and can be expressed as:

$$f_\varepsilon = f \otimes \eta_\varepsilon = \sum_{i=1}^{N} f_i(x_i, y_i, z_i, t) \frac{1}{\varepsilon^3 \pi^{\frac{3}{2}}} exp\left[- \left(\frac{d_i}{\varepsilon}\right)^2 \right] \tag{7}$$

where, N is the number of blade sections of wind turbine blades; (x_i, y_i, z_i) is the coordinate of i-th actuator point; d_i is the distance from actuator point to projection point; ε is the projection width, $\varepsilon \approx 2\Delta x$ is recommended by Troldborg (Troldborg et al., 2007), where Δx is the mesh size near wind turbine. In addition to wind turbine blades, nacelle and tower are also considered and modeled by ALM.

2.3. Hydrodynamic modeling

The hydrodynamics of FOWT is predicted by a two-phase CFD solver naoe-FOAM-SJTU, which is a solver developed on the basis of OpenFOAM for the hydrodynamics of floating structures (with mooring lines). By integrating the ALM of wind turbine aerodynamics into this solver, the fully coupled aero-hydrodynamics of FOWT is able to predict, namely FOWT-UALM-SJTU. The ability of naoe-FOAM-SJTU to accurately predict hydrodynamic responses of floating structures subjected to various complicated environments has been comprehensively verified (Cao et al., 2013; Cao and Wan, 2014; Shen et al., 2012a; Wang et al., 2019; Zhao and Wan, 2015). The naoe-FOAM-SJTU is composed of several modules, including a numerical tank for wave generation and absorption, a 6DoF motion module for hydrodynamic responses of floating structures, and a mooring system for limitation of displacements of floating structures. The incompressible Navier-Stokes equations are solved in this solver, which are discretized by FVM. A dynamic mesh technique is utilized to handle the motions of floating structures (Shen et al., 2012b). In order to capture the free surface, the volume of fluid (VOF) method with bounded compression technique is used. The VOF transport equation is as follows:

$$\frac{\partial \alpha}{\partial t} + \nabla \bullet \left((U - U_g)\alpha\right) + \nabla \bullet (U_r(1-\alpha)\alpha) = 0 \tag{8}$$

where, U is the velocity of flow field; U_g is the velocity of grid nodes; α is the volume fraction representing the relative proportion of fluid in each cell, which is defined as:

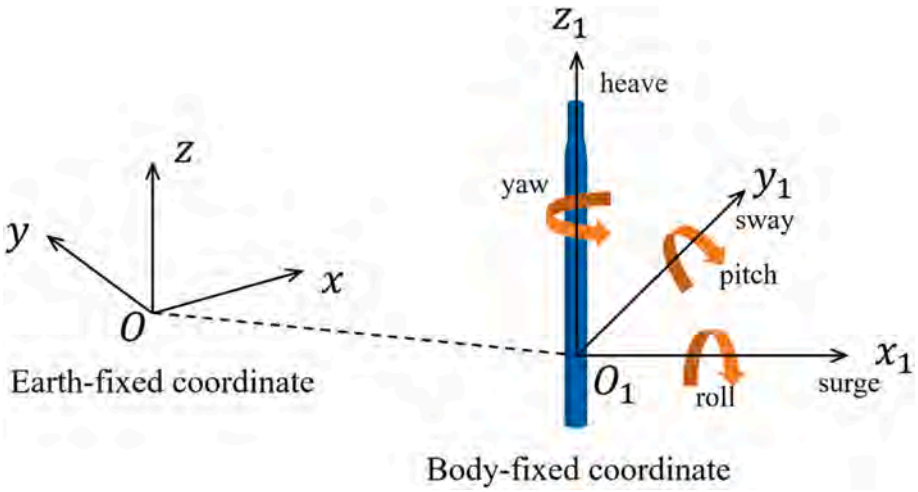

Fig. 2. Two coordinate systems of floating platform.

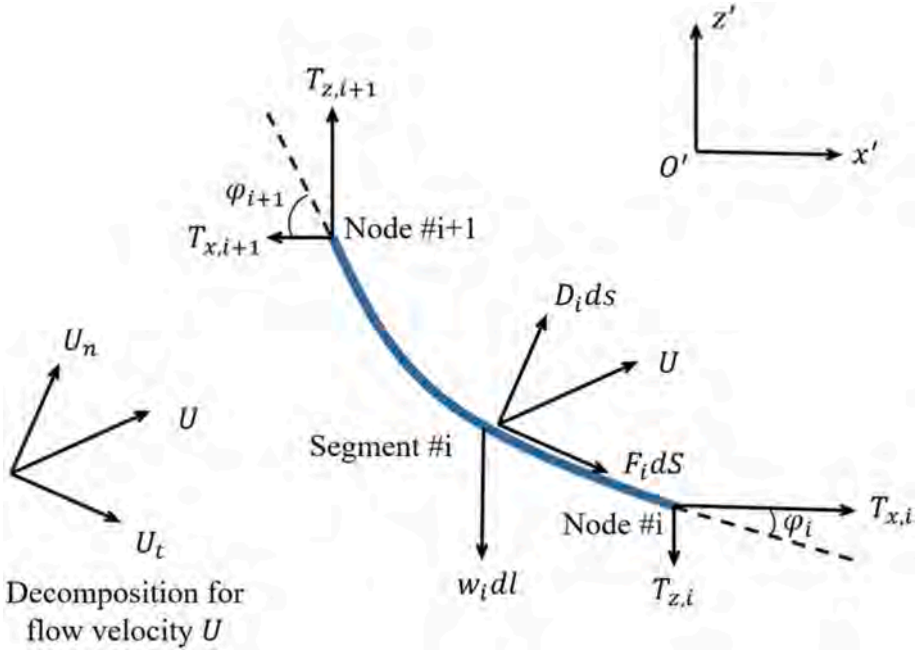

Fig. 3. Force analysis on one segment of mooring cables.

$$\begin{cases} \alpha = 0 & \text{air} \\ \alpha = 1 & \text{water} \\ 0 < \alpha < 1 & \text{interface} \end{cases} \tag{9}$$

The fluid density ρ and dynamic viscosity μ can be described as:

$$\rho = \alpha\rho_l + (1-\alpha)\rho_g \tag{10}$$

$$\mu = \alpha\mu_l + (1-\alpha)\mu_g \tag{11}$$

where, the subscripts l and g refer to the liquid and gas, respectively.

For the 6DoF motion module, the 6DoF equations of floating platform are solved to predict its hydrodynamic responses. The external loads, i.e., the wind loads, wave loads and mooring loads are considered in the 6DoF equations. Two coordinate systems are used, one is earth-fixed coordinate system and the other is body-fixed coordinate system, as shown in Fig. 2. The motion equations are solved in body-fixed coordinate system while the forces are calculated in earth-fixed coordinate system. Therefore, a transformation of data between these two coordinate systems is required. For the dynamic responses of FOWT under combined wind-wave condition, the aerodynamic loads of wind turbine will be transferred to floating platform through tower, and the motions of floating platform are altered. In order to account for the impacts of wind turbine on motions of floating platform, aerodynamic loads of wind turbine predicted by ALM is integrated into the force equations of floating platform. More specifically, the aerodynamic forces and moments are imposed on the gravity center of floating platform. Note that the added velocity on wind turbine induced by platform motions is considered in calculations of aerodynamic loads, and it can be expressed by:

$$U_{motion,i} = [J](U_c + \omega_c \times (x_i - x_c)) \tag{13}$$

where, $[J]$ is a transformation matrix from body-fixed coordinate to earth-fixed coordinate; U_c and ω_c are the translational velocity and angular velocity of rotating center; x_c is the location of rotating center.

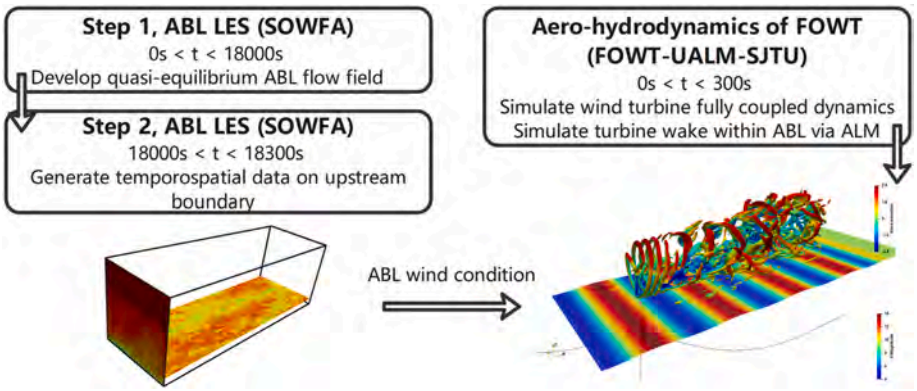

Fig. 4. Procedure of simulated atmospheric inflow wind condition for FOWT.

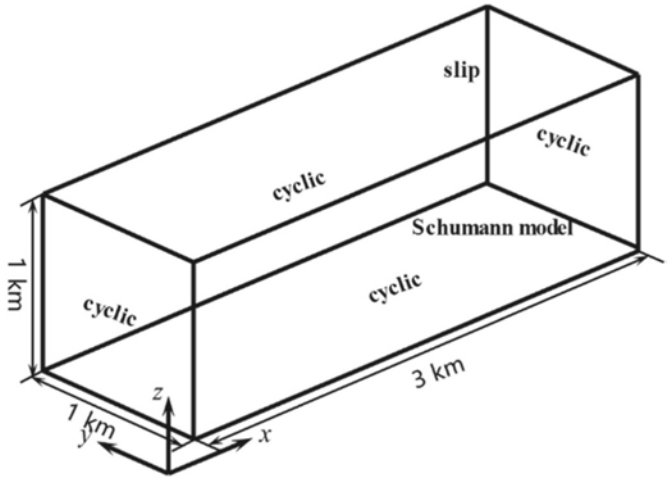

Fig. 5. Computational domain and boundary conditions for generation of atmospheric wind field.

2.4. Mooring system modeling

The piecewise extrapolating method (PEM) is employed to calculate the forces of mooring cables, which is a quasi-static method that the mooring cables are divided into many segments. According to static analysis of one of segments in Fig. 3, the static equations of this segment are established:

$$\begin{cases} T_{x,i+1} - T_{x,i} - F_i ds \bullet cos\ \varphi_{i+1} - D_i ds \bullet sin\ \varphi_{i+1} = \rho g A \Delta z^{'} \bullet cos\ \varphi_{i+1} \\ T_{z,i+1} - T_{z,i} - F_i ds \bullet sin\ \varphi_{i+1} + D_i ds \bullet cos\ \varphi_{i+1} - w_i dl = \rho g A \Delta z^{'} \bullet sin\ \varphi_{i+1} \end{cases} \tag{9}$$

where, T is mooring force; φ is an angle between mooring force and its horizontal component; F and D are tangential and normal forces of fluid on mooring cables, respectively; dl and ds are lengths of this segment before and after stretching; w is wet weight of this segment in water; ρ is fluid density; g is gravitational acceleration; A is cross sectional area of this segment; $\Delta z^{'}$ is vertical distance between two nodes of segment. The forces of fluid on mooring cables can be calculated by Morison equations, and the forces and shapes of mooring cables are determined by integrating boundary conditions of mooring cables.

2.5. Atmospheric turbulence inflow modeling

The atmospheric inflow wind condition is simulated and generated by LES with sufficient simulation duration in SOWFA simulation framework (Fleming et al., 2014), which is a LES framework proposed by National Renewable Energy Laboratory (NREL) and developed on the basis of OpenFOAM. Compared to the turbulence wind model, the generated atmospheric inflow wind condition is more physical and realistic, as this wind condition is simulated by LES with sufficient duration. In the previous studies for bottom-fixed wind turbines immersed in ABL wind field, the SOWFA simulation framework has been widely verified and applied (Chanprasert et al., 2022; Churchfield et al., 2012; Ning and Wan, 2019; Yang et al., 2022). In a hexahedron computational domain without wind turbines, cyclic boundary condition is applied on four vertical boundaries to allow flow field exiting from downstream enters upstream. With the help of sufficient simulation duration, the steady wind at initial time instant reaches quasi-equilibrium atmospheric turbulence wind. The desired wind speed at specific level (i.e., hub level of wind turbine) is guaranteed by adjusting the background pressure gradient. It is noticeable that the molecular viscosity is not considered due to the characteristic of high Reynolds number in atmospheric wind field. Details of governing equations in SOWFA framework for simulation of atmospheric inflow can be found in literature (Churchfield et al., 2012).

Once the wind field reaches quasi-equilibrium, the temporospatial data on upstream plane are saved as atmospheric inflow wind condition for simulation of FOWT, as shown in Fig. 4. In FOWT-UALM-SJTU framework, the fully coupled wind turbine aerodynamics, floating platform hydrodynamics and mooring system dynamics are simulated under combined wind-wave condition. Note that this procedure is only used for FOWT under atmospheric inflow wind condition, uniform and shear wind inflows are directly specified on the upstream boundary of computational domain containing FOWT.

3. Validation and verification

3.1. Generation of atmospheric inflow wind condition

Fig. 5 shows the computational domain and boundary conditions of simulation of atmospheric wind field. The length, width and height of computational domain are 3 km, 1 km and 1 km, respectively. The cyclic boundary is applied for four vertical boundaries, which means the data on downstream boundary is circularly transmitted to upstream boundary. The geostrophic wind at the level of top boundary is considered horizontal, consequently, slip boundary condition is used on top boundary. For the bottom boundary, the Schuman wall model (Schumann, 1975) is applied to calculate the surface shear stress, and the representative sea surface of roughness length of 0.001 is used. Our previous efforts suggested that the vertical scale of mesh near bottom boundary needs to be smaller to avoid the undesirable wave height when the generated atmospheric inflow is used for the two-phase simulation of FOWT. Therefore, the linear expansion of vertical scale of mesh from bottom to top is employed, although the application of surface shear stress model allows uniform spacing of mesh in the height

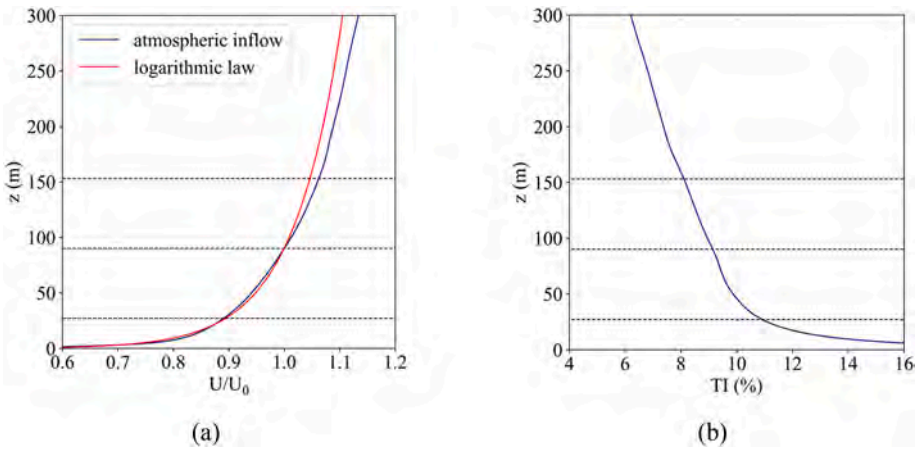

Fig. 6. Time-averaged profiles of the simulated ABL wind field: (a) wind speed; (b) turbulence intensity. Three black dashed lines denote heights of rotor top, center and bottom.

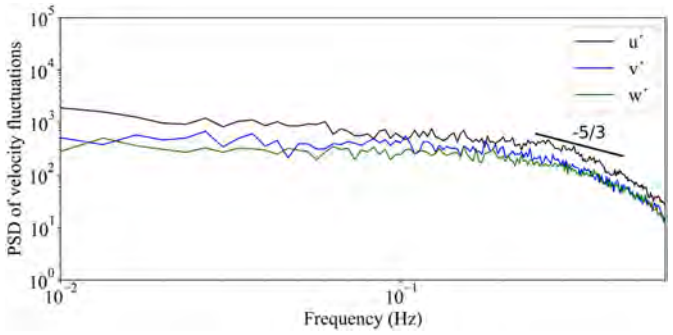

Fig. 7. Power spectrum of wind speed fluctuations at hub level.

direction of the computational domain (Chanprasert et al., 2022). The mesh resolution along x- and y-axes are both 10m, while the linear expansion is used along z-axis, resulting in a vertical resolution of 0.24m near bottom of the mesh. The multiscale turbulence structures exist in atmospheric wind field, and the largest scale and smallest scale are of the order of km and mm, respectively. There is no doubt that larger computational domain and higher mesh resolution are more conducive to capturing multiscale turbulence structures, the computational cost is expensive and unaffordable for our current work. What's more, the similar computational domain and mesh resolution are employed by previous studies (Churchfield et al., 2012; Ning and Wan, 2019) and have been proven sufficient capturing turbulence structures in atmospheric wind field.

At the initial time instant, the steady wind with wind speed of 11.4 m/s fills the computational domain. The simulation time and time step are 18000s and 0.2s, note that this simulation time is sufficient to drive the steady wind to reach quasi-equilibrium atmospheric wind field. After the simulation of 18000s is completed, an additional 300s of continue simulation is conducted and data of each time step on upstream boundary are saved as atmospheric inflow wind condition for the two-phase simulation of FOWT. The time step is reduced to 0.02s to obtain temporally high-resolution data.

The last 300s data on upstream boundary is saved as atmospheric inflow wind condition of FOWT, consequently, validation of this simulated wind condition is necessary. Fig. 6 shows time-averaged wind speed profile and turbulence intensity profile of the atmospheric wind field. The speed profile is normalized by rated wind speed of 11.4 m/s. The wind speed at hub level is well consistent with rated wind speed of 11.4 m/s, and the characteristic of wind shear due to friction of sea surface is produced. What's more, the simulated wind speed profile matches logarithmic law very well, especially for the level below hub height. The logarithmic law is also used in this work as the shear wind inflow condition, its expression is as follows:

$$\overline{u}(z) = \frac{u_*}{\kappa} ln\left(\frac{z}{z_0}\right) \tag{10}$$

where, $\overline{u}(z)$ is time-averaged wind speed over a plane at height of z; $\kappa = 0.4$ is von Karman constant; $z_0 = 0.001$ is roughness length. To match the desired wind speed of 11.4 m/s at hub level, the friction velocity is determined as 0.398.

The turbulence intensity presented in Fig. 6b is defined by:

$$TI(z) = \frac{\sqrt{\overline{(u(z,t) - \overline{u}(z))^2}}}{\overline{u}(z)} \tag{11}$$

where, the overbar denotes time average; $u(z,t)$ is wind speed at time instant t over the z level plane. As expected, the turbulence intensity of this atmospheric wind field decreases with increase of height. The turbulence intensities at rotor top, center and bottom are 8.10%, 9.14% and 10.93%, respectively, resulting in a difference of 2.83% over the height range of wind turbine rotor.

Fig. 7 presents the power spectrum density (PSD) of wind speed fluctuations at hub level. The spectrums of wind speed components decrease with increasing frequency, indicating that the large-scale turbulence structures in low-frequency region contains stronger turbulence energy. In the transition region from high frequency to low frequency (i.e., 0.2Hz-0.4Hz), the spectrums of fluctuations of three wind speed components illustrates a consistent with $-5/3$ slope, suggesting that the energy cascade from large-scale turbulence structures to small-scale turbulence structures in atmospheric wind field are well reproduced by the LES.

3.2. Wake modeling of FOWT

The coupled aero-hydro-moor performance of FOWT excited by incident wind-wave conditions is a complex issue. The ability of in-house solver FOWT-UALM-SJTU to accurately predict aero-hydro-moor responses of FOWT was comprehensively validated by Cheng et al. (2019) by sequentially comparing unsteady aerodynamics of wind turbine, free decay of floating platform and hydrodynamics of floating platform under regular wave with results predicted by other numerical methods. After that, this solver was employed for studies of aero-hydrodynamics of FOWT and wake interactions between two FOWTs (Huang and Wan, 2019; Huang et al., 2023b). Due to the investigation of wake characteristics of FOWT is an interest in present

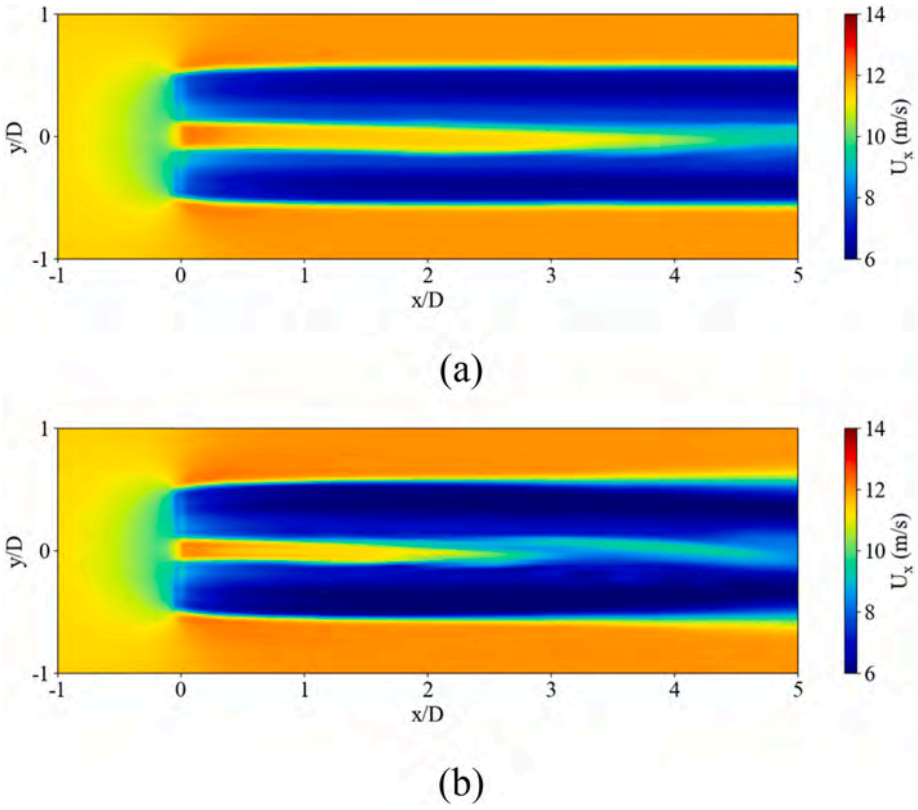

Fig. 8. Time-averaged streamwise velocity contours in hub level plane predicted by: (a) in-house solver FOWT-UALM-SJTU; (b) SOWFA.

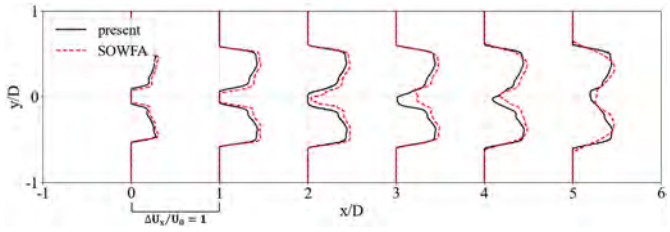

Fig. 9. Wake deficit at different downstream distances.

work, the validation of this solver for modeling wind turbine wakes is performed.

The NREL 5 MW wind turbine is utilized as the wind model, and for simplicity, only the wind turbine blades are considered and modeled. The inflow wind condition is uniform inflow with wind speed of 11.4 m/s, and the corresponding rotor speed is 12.1rpm. Note that the grid, time step and simulation time in our solver are the same as those of SOWFA. Fig. 8 shows the time-averaged streamwise velocity contours in hub level plane predicted by in-house solver FOWT-UALM-SJTU and SOWFA. The significantly decreased velocity behind wind turbine is observed, and a long-distance high-speed airflow belt appears at hub center due to the absence of hub and nacelle. It seems that the wake deficit predicted by FOWT-UALM-SJTU is weaker compared to that of SOWFA.

In order to make a quantitative comparison, Fig. 9 presents the wake deficit at different downstream distances. The velocity deficit is determined by:

$$V_d = \frac{U_0 - U_w}{U_0} \tag{12}$$

where, U_0 is the freestream velocity; U_w is the mean streamwise velocity in the wake. The velocity deficit exhibits a bimodal distribution in both CFD frameworks, and the location of maximum velocity deficit is shifted from near the blade tip to the hub center with increasing downstream distances. The wake deficit is still strong even at downstream 5D because of the limited contribution of uniform wind inflow to wake recovery of wind turbine. Consistent with above analysis in velocity contours, the wake deficit in in-house solver FOWT-UALM-SJTU is slightly weaker. Overall, the wake deficit predicted by in-house solver FOWT-UALM-SJTU shows a good agreement with that of SOWFA. In addition, the wake width increases when wake travels downstream, which is referred to wake expansion. Note that in here, the wake boundary is approximately determined when wake deficit reaches 0. The wake width predicted by in-house solver FOWT-UALM-SJTU is in line with that of SOWFA. Consequently, the ability of in-house solver FOWT-UALM-SJTU for predicting wake characteristics of wind turbine is sufficient.

4. Simulation details

4.1. FOWT model

A spar buoy FOWT is utilized as the research object in this work, which is composed of a NREL 5 MW wind turbine, a OC3 Hywind spar platform and a mooring system. The NREL 5 MW wind turbine is a conventional upwind three-blade wind turbine, and its rated power and rated wind speed are 5 MW and 11.4 m/s, respectively. Although rotor torque controller and blade pitch controller are equipped with this wind turbine, the control of wind turbine is not the interest of our work and is not considered. Therefore, rotor speed of FOWT is a constant in process of numerical simulations and determined by initial wind speed at hub level. Due to the NREL 5 MW wind turbine is representative, detailed definitions of this wind turbine are not presented here but can be found in reference (Jonkman et al., 2009).

The OC3 Hywind spar platform is employed to carry the wind turbine. Note that the structure of this floating platform is uncomplicated, but high requirement of water depth of its positioned sea area is needed

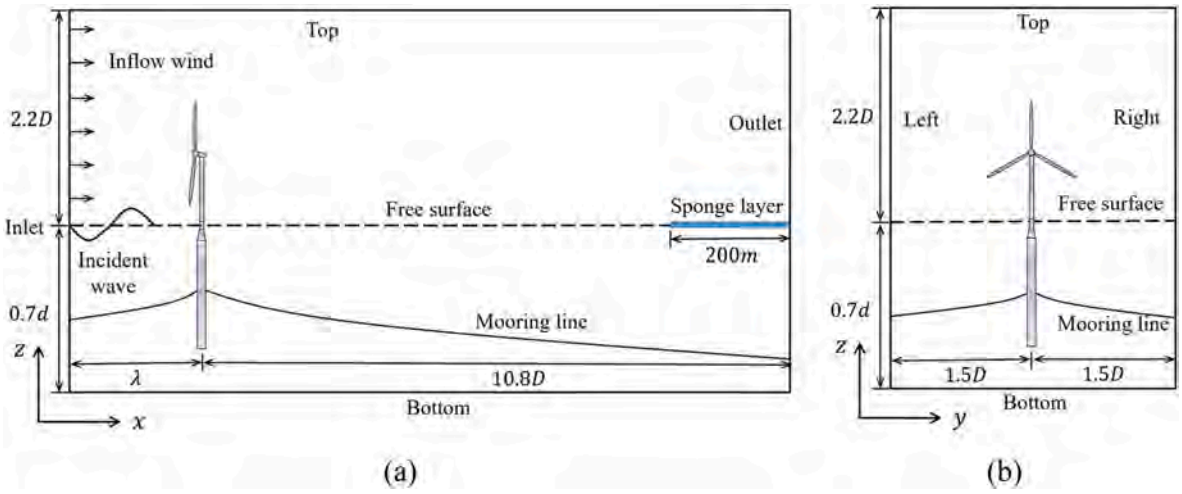

Fig. 10. Computational domain of the FOWT: (a) xz plane; (b) yz plane.

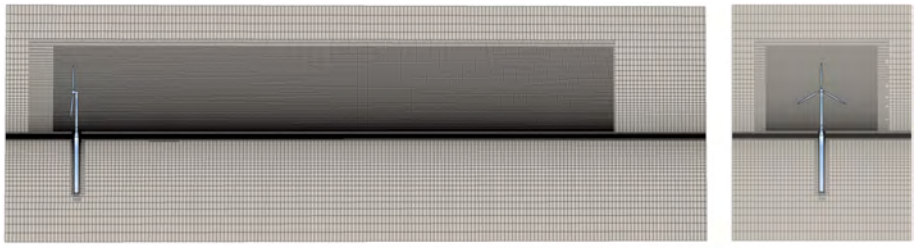

Fig. 11. Mesh generation of computational domain of FOWT: (a) xz plane; (b) yz plane.

(draft and water depth of OC3 Hywind spar platform are 120m and 320m). Three mooring cables with 120° adjacent angle are connected on the floating platform to limit hydrodynamic responses of FOWT and guarantee its safe operation. More detailed parameters of OC3 Hywind spar platform and mooring system can refer to literatures (Jonkman, 2010; Jonkman and Musial, 2010).

4.2. Computational setup

The two-phase CFD simulation of FOWT subjected to wind-wave condition is computationally expensive, although the wind turbine is modeled by ALM. Determination of computational domain depends on how to save computational cost within reasonable accuracy of results. As illustrate in Fig. 10, a cuboid domain is utilized for coupled aero-hydrodynamic simulation of FOWT, in which its three dimensions are 1512m (x-axis), 384m (y-axis) and 504m (z-axis), respectively. It is noteworthy that width and height of the computational domain are the same as those of Huang and Wan (2019), whereas the length in this work is longer with aim of capturing and analyzing wakes of FOWT. The FOWT is located at downstream 150m (appropriate one wave length $\lambda =$ 156m) from inlet boundary. In order to save computational cost, depth of water-phase is set to 224m (70% of actual water depth $d = 320$m). The height of air-phase is 280m (about 2.2D, D = 126m is rotor diameter) and is sufficient for development and expansion of wind turbine wakes. To absorb wave reflection, a rectangular sponge layer with length of 200m is used at upstream of outlet boundary.

The sizes of background mesh in x- and y-axes directions are both 8m, while its size along z-axis is linearly variable to capture free surface and restrict total grid number, as shown in Fig. 11. The vertical size of background mesh near free surface is 2m, and it linearly expands up to 20m at top and bottom boundaries. To identify and capture free surface, as well as capture development and evolution of wind turbine wakes, two-level mesh refinement is adopted for domain of free surface and wind turbine wakes. What's more, the grids around floating platform are also refined. According to related references (Huang and Wan, 2019; Xu et al., 2023a, 2023b; Ning and Wan, 2019), mesh resolution in this work is sufficient to guarantee the accuracy of numerical results and capture the wake characteristics of wind turbine. As a result, the total grid number is 11.8 million.

For the boundary conditions, combined incident wind-wave is imposed at inlet boundary. The normal zero gradient condition is applied on outlet boundary. The free-slip condition is utilized for top boundary, and also for bottom boundary due to the fact that the bottom of computational domain is not actual seabed. What's more, the symmetrical condition is used on left and right boundaries, and no-slip condition is adopted on surface of floating platform.

To study the effects of inflow winds on dynamic responses and wake characteristics of FOWT, three inflow wind conditions are used: uniform inflow, shear inflow and atmospheric inflow simulated by LES. Note that logarithmic law is utilized for shear wind, and the friction velocity is determined by matching mean wind speed profile of atmospheric inflow (see Fig. 6a and Equation (10)). The wind speed at hub level is 11.4 m/s for these three inflow winds, and the corresponding rotor speed is 12.1rpm. The incident wave in this work refer to Zhao et al. (Zhao and Wan, 2015), in which first-order Stokes wave with wave height of 3.66m and wave period of 9.7s is selected. The direction of combined wind-wave is positively aligned with the x-axis, and also parallel to direction of surge motion of platform.

The time step $\Delta t = 0.01$s is selected in simulation of FOWT as suggested by Huang et al. (2019), they emphasized that this time step is suitable for CFD simulation of OC3 Hywind spar platform and provides sufficient assurance for the convergence of aerodynamic loads. The simulation time is 30 wave periods based on a comprehensive consideration of stability of results and computational cost. The coupled

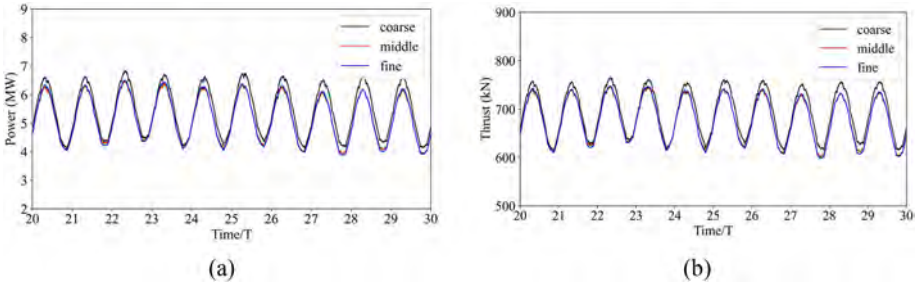

Fig. 12. Aerodynamic performance of FOWT under different mesh resolutions: (a) power; (b) thrust.

Table 1
Statistics of aerodynamic power and thrust for different mesh resolutions, including values of maximum, minimum, mean.

Case	Mesh resolution near wind turbine	Power (MW)		
		Max	Min	Mean
coarse	$2\sqrt{2}m \times 2\sqrt{2}m \times 2\sqrt{2}m$	6.84 (6.88%)	4.09 (7.63%)	5.44 (6.67%)
middle	$2m \times 2m \times 2m$	6.46 (0.94%)	3.94 (3.68%)	5.18 (1.57%)
fine	$\sqrt{2}m \times \sqrt{2}m \times \sqrt{2}m$	6.40	3.80	5.10
Case	Mesh resolution near wind turbine	Thrust (kN)		
		Max	Min	Mean
coarse	$2\sqrt{2}m \times 2\sqrt{2}m \times 2\sqrt{2}m$	765 (2.54%)	611 (2.17%)	692 (2.06%)
middle	$2m \times 2m \times 2m$	746 (−0.13%)	602 (0.69%)	678 (0%)
fine	$\sqrt{2}m \times \sqrt{2}m \times \sqrt{2}m$	747	598	678

aero-hydrodynamic simulations of FOWT are conducted on high-performance computing platform of Computational Marine Hydrodynamics Lab (CMHL) at Shanghai Jiao Tong University. The processors of each node are 2 × Intel Xeon Gold 5120 (14 Cores, 2.20Ghz) with 128 GB memory. Five nodes are used for each case and the CPU time is 363h.

5. Results and discussions

5.1. Mesh convergence study

The mesh convergence study is first conducted to assess the influence of mesh resolution on numerical results. Three different mesh resolutions, namely coarse, middle and fine are utilized. The mesh resolutions near wind turbine are $2\sqrt{2}m \times 2\sqrt{2}m \times 2\sqrt{2}m$, $2m \times 2m \times 2m$ and $\sqrt{2}m \times \sqrt{2}m \times \sqrt{2}m$, respectively. In order to save the computational costs, the wake region of FOWT is not refined. The total mesh number of the three cases are 1.99 million, 4.47 million and 10 million. The wind inflow is uniform wind with wind speed of 11.4 m/s, and the incident wave, simulation time and time step are consistent with the description in Section Computational setup. Fig. 12 shows the power and thrust of FOWT under three different mesh resolutions, and a quantitative comparison is summarized in Table 1. Compared to the results of fine case, the power and thrust of coarse case show a small discrepancy. With the mesh resolution near wind turbine increases to $2m \times 2m \times 2m$, the power and thrust of FOWT exhibits a negligible difference. Consequently, in order to comprehensively consider numerical accuracy and computational costs, the mesh generation of middle case is employed for the fully coupled aero-hydrodynamics and wakes of FOWT.

5.2. Aerodynamic performance

The aerodynamic performance of FOWT including power and thrust under three wind inflows is firstly examined, as shown in Fig. 13. It is noticeable that the time is normalized by wave period T = 9.7s, and last 10 wave periods of time histories are presented. There is no doubt that aerodynamic performance of FOWT is significantly influenced by platform motions, which called unsteady aerodynamics. Thus, time histories of power and thrust show a periodic variation with incident wave for all inflow wind conditions. The shear of shear wind inflow is not strong due to the low roughness length on sea surface, specifically, difference of wind speed between rotor-top and rotor-bottom is 1.7 m/s (15% of wind speed at hub level). Consequently, the significant difference of

Table 2
Statistics of aerodynamic power and thrust for different inflow wind conditions, including values of maximum, minimum, mean, root mean square and standard deviation.

Case	Power (MW)				
	Max	Min	Mean	Rms	Std
uniform	6.46	3.94	5.18	5.23	0.76
shear	6.39	3.86	5.10	5.16	0.76
atmospheric	6.67	3.61	5.07	5.13	0.77
Case	Thrust (kN)				
	Max	Min	Mean	Rms	Std
uniform	746	602	678	679	44
shear	743	598	674	675	44
atmospheric	761	579	672	673	46

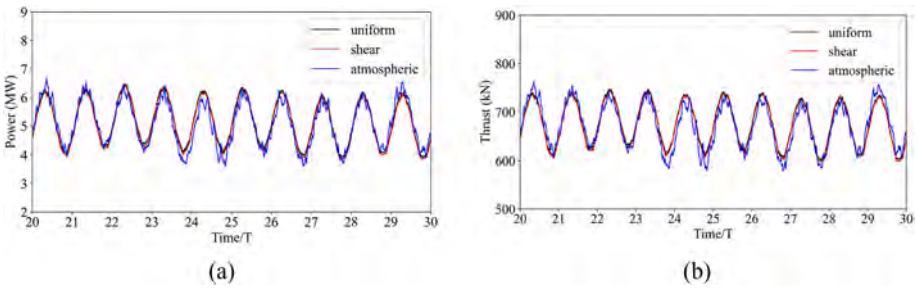

Fig. 13. Aerodynamic performance of FOWT under three wind inflows: (a) power; (b) thrust.

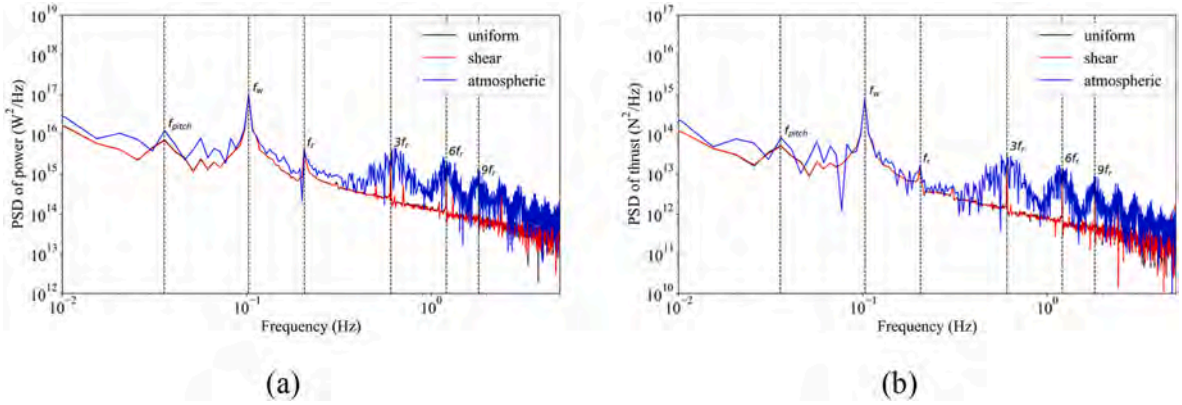

Fig. 14. Power spectrum of aerodynamic performance of FOWT under three wind inflows: (a) power; (b) thrust.

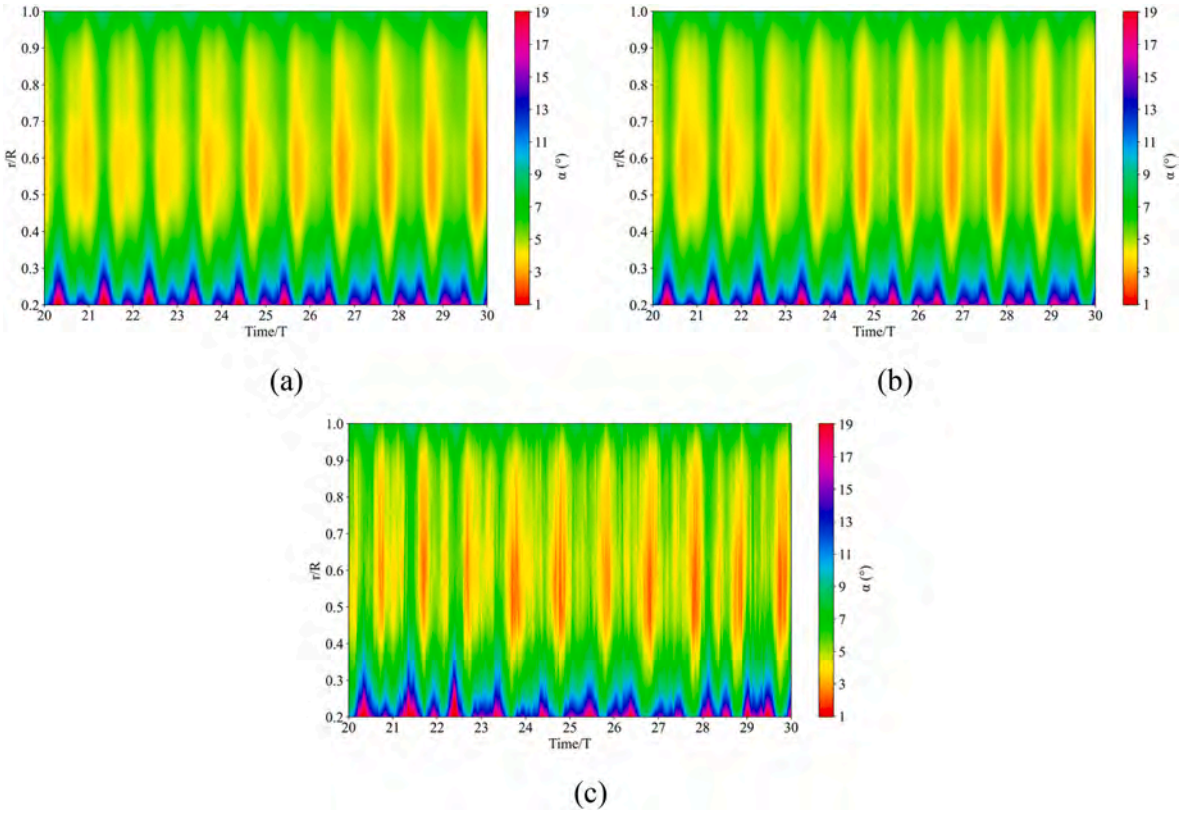

Fig. 15. Spatiotemporal distribution of angle of attack under three wind inflows: (a) uniform; (b) shear and (c) atmospheric.

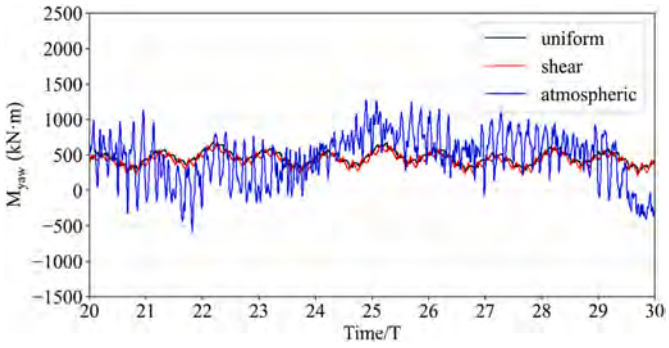

Fig. 16. Yaw moment of FOWT under three wind inflows.

Table 3
Statistics of yaw moment for different inflow wind conditions, including values of maximum, minimum, mean, root mean square and standard deviation.

Case	Yaw moment (kN·m)				
	Max	Min	Mean	Rms	Std
uniform	686	267	458	466	88
shear	662	202	430	438	87
atmospheric	1271	−569	463	581	351

aerodynamic performance between uniform inflow and shear inflow is not observed. Due to the tower is considered and modeled by ALM, some minor decreases in time histories of uniform inflow and shear inflow called tower effects are visible if we take a closer look. Power and thrust of FOWT in atmospheric inflow scenario are more unstable, obviously,

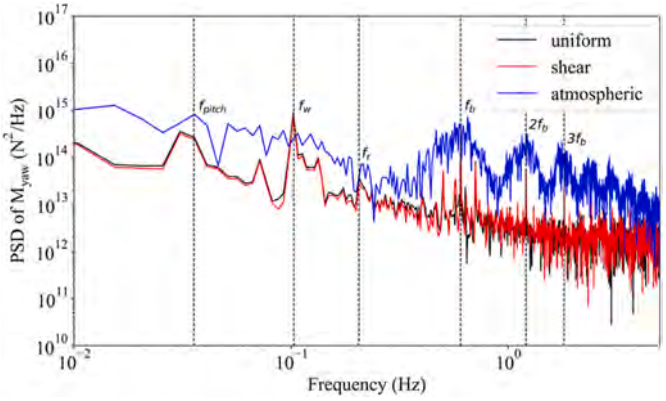

Fig. 17. Power spectrum of yaw moment of FOWT under three wind inflows.

this can be attributed to turbulence in atmospheric wind inflow.

The statistics of power and thrust composed of values of maximum, minimum, mean, root mean square and standard deviation are summarized in Table 2. A minor difference in power output for the three wind inflows is observed. It is noticeable that maximum of power is enhanced while minimum of power is suppressed when the FOWT under atmospheric inflow. The variation amplitude of power of atmospheric inflow is 3.06 MW, which is intensely greater than 2.52 MW of uniform inflow and 2.53 MW of shear inflow. The standard deviation of power under these inflow conditions is almost identical, revealing that the power output mainly depends on platforms motions, then followed by inflow wind conditions. However, this conclusion should be carefully treated if milder sea conditions and floating platform with better hydrodynamic performance are utilized. The same conclusion can be addressed for the analysis of thrust output.

The PSD of above two quantities is illustrated in Fig. 14. As depicted in Fig. 13, aerodynamic performance of FOWT exhibits unsteady feature due to inflow wind conditions of wind turbine are changed by wave-excited platform motions. Therefore, for these inflow wind conditions, the peak of incident wave frequency f_w is significant. The natural frequency of pitch f_{pitch} is also visible, indicating that the impacts of platform pitch motion on aerodynamic performance are notable. In addition, the peaks of rotor revolution frequency f_r and its harmonics are evident. In high frequency region, the difference in power spectrum among these inflow wind conditions is obvious. Compared to uniform and shear inflows, the PSD of atmospheric inflow is more intense when the frequency is greater than 0.3Hz, suggesting that more energy exist in high frequency region because of high-frequency small-scale turbulence structures in atmospheric inflow. Consequently, fatigue load of FOWT

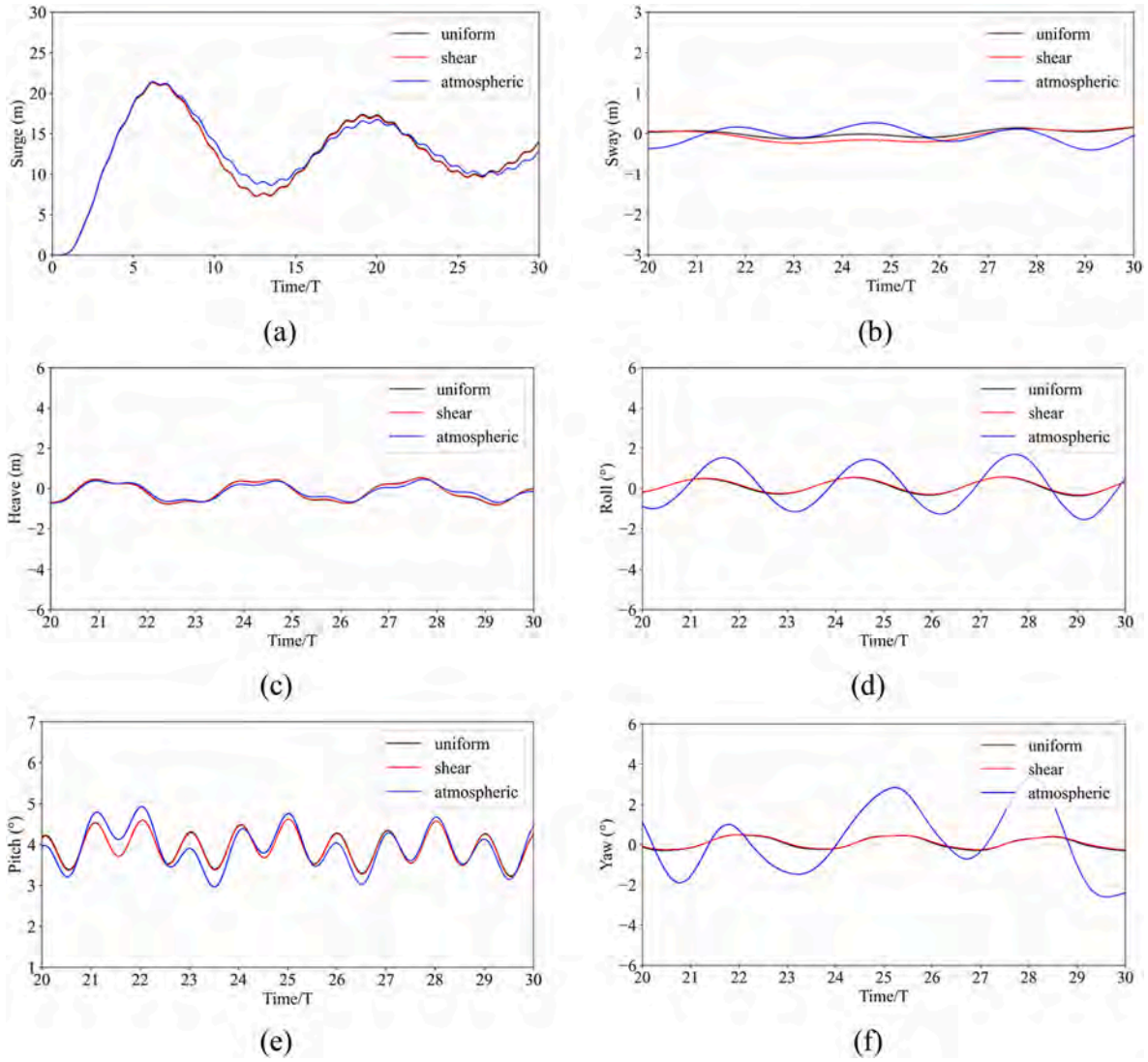

Fig. 18. Platform motions of FOWT under three wind inflows.

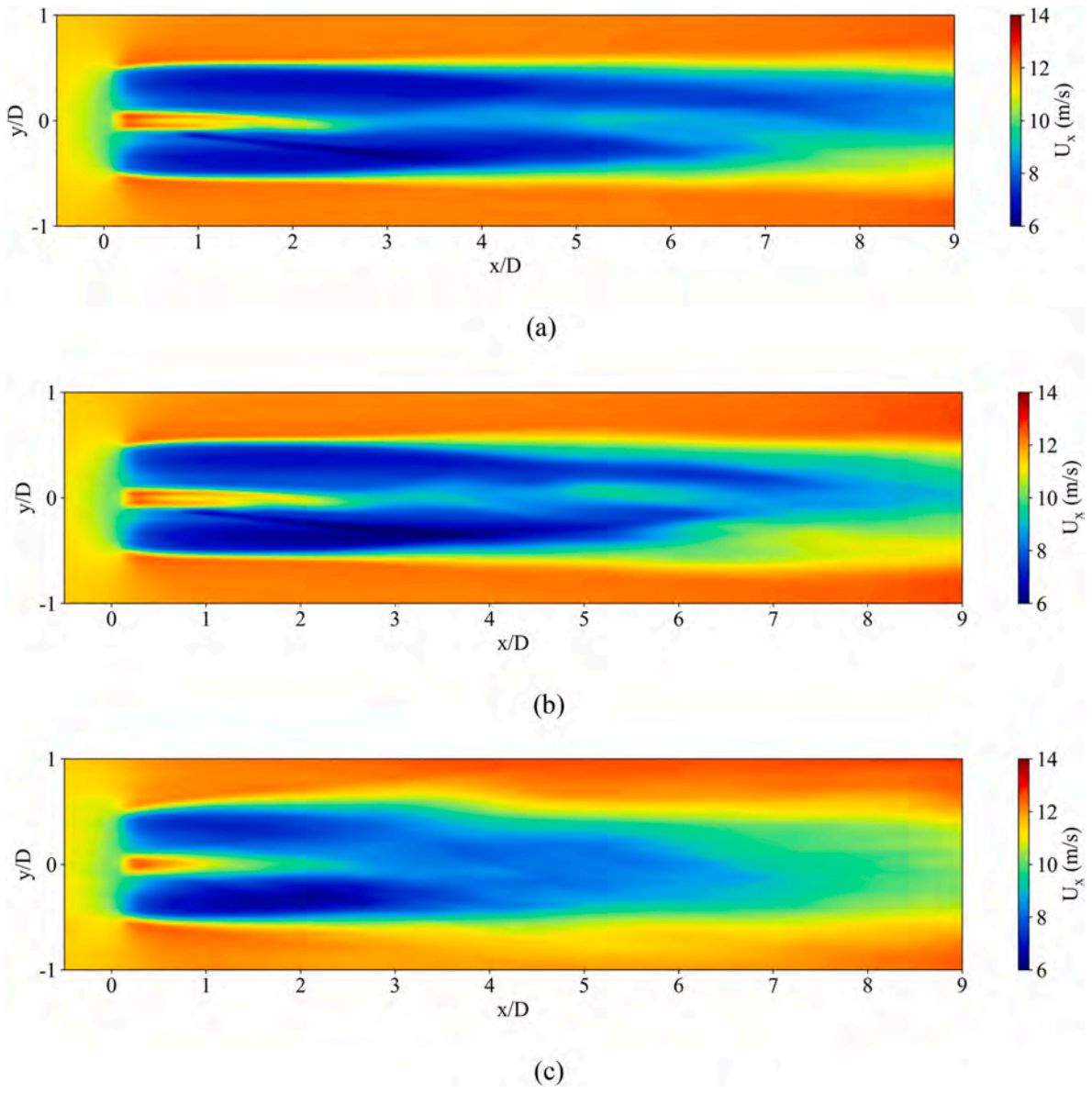

Fig. 19. Time-averaged streamwise velocity contours in hub level plane for different inflow wind conditions: (a) uniform; (b) shear and (c) atmospheric.

under atmospheric inflow maybe severe and more efforts on it are suggested.

5.3. Angle of attack

The discrepancies of aerodynamic performance among the three inflow wind conditions are attributed to the change of angle of attack, as illustrated in Fig. 15. It is found that the angle of attack of FOWT subjected to uniform inflow shows a remarkable periodic variation, which may be resulted from platform motions. Hence, to pursue better aerodynamic performance, the unsteady change of the angle of attack needs to be considered in blade design of FOWT. The limited difference between uniform inflow and shear inflow is observed. In addition to the periodic variation similar to that of uniform inflow, the angle of attack of atmospheric inflow also presents a more unstable trend. The decreased angle of attack is clear at the middle of blade, and the increased angle of attack is evident near the blade root. This observation suggests that the spatiotemporal variation of angle of attack in atmospheric scenario is more drastic and brings greater challenges to blade design of FOWT.

5.4. Yaw moment

In terms of aerodynamic responses, the yaw moment of FOWT is also presented and analyzed, as shown in Fig. 16. For the uniform and shear inflows, the yaw moment of FOWT shows a periodic variation with incident wave. What's more, in an incident wave period, the periodic variation of yaw moment with smaller period corresponding to blade passage is also observed. It is noteworthy that the period of blade passage is one-third of period of rotor revolution, since the NREL 5 MW wind turbine with three blades is selected as the computational model. The variation of yaw moment in shear scenario is more pronounced compared to that in uniform scenario, which can be attributed to the presence of shear characteristic in shear inflow. Different from uniform and shear inflows, the yaw moment in atmospheric scenario is significantly sophisticated and its periodic variation with incident wave is not observed. For uniform and shear inflows, the yaw moment varies around 500 kN m, while it changes from −500 kN m to over 1000 kN m for atmospheric inflow.

The quantitative analysis of yaw moment is summarized in Table 3. Consistent with above analysis for aerodynamic power and thrust, the

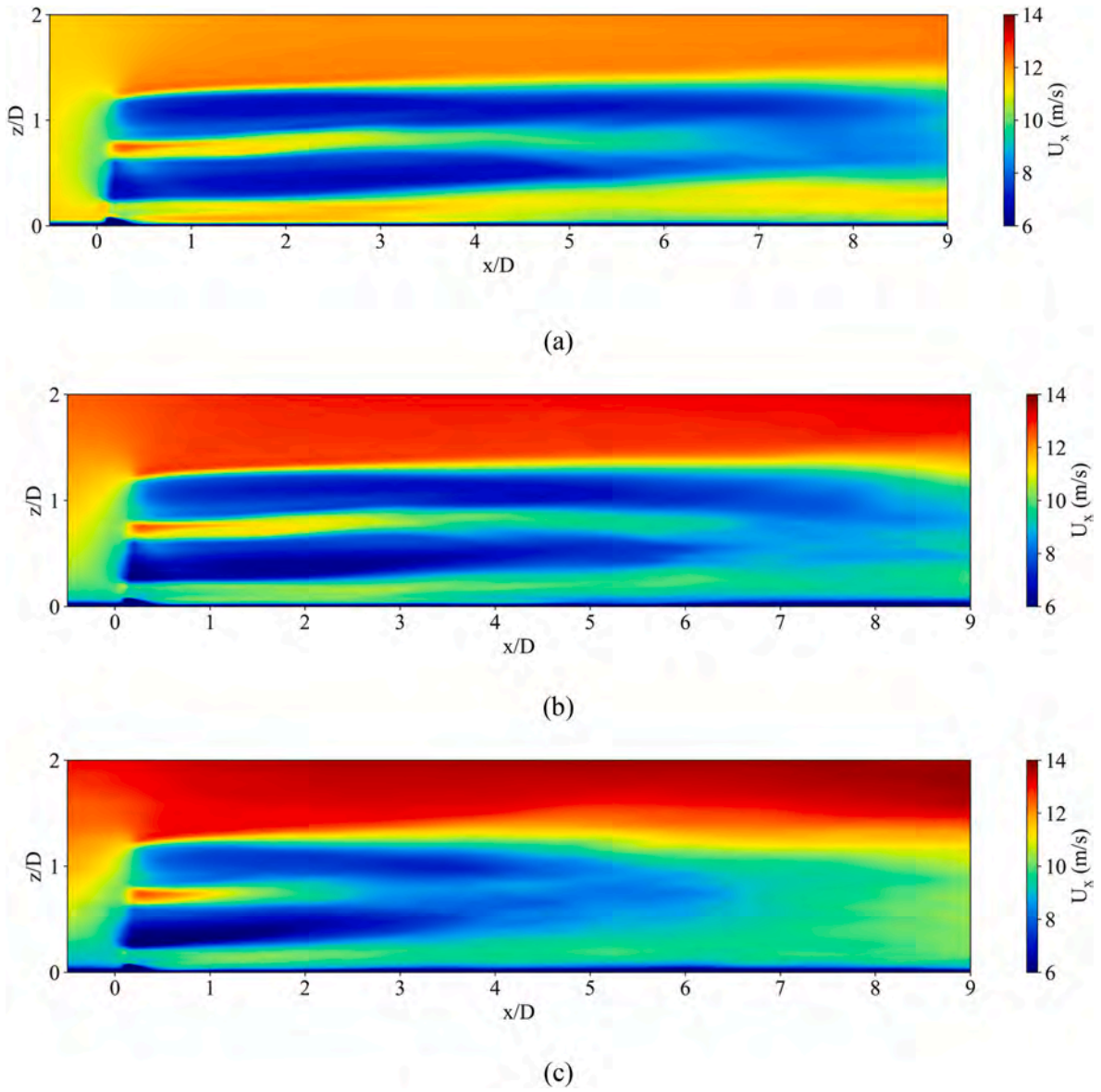

Fig. 20. Time-averaged velocity contours in vertical plane through rotor center for different inflow wind conditions: (a) uniform; (b) shear and (c) atmospheric.

difference of yaw moment between uniform and shear inflows is small due to the insignificant shear feature in shear wind inflow. The varying amplitude of yaw moment in uniform and shear scenarios are 419 kN m and 460 kN m, while this value is amplified to 1840 kN m in atmospheric scenario. What's more, the standard deviation of yaw moment under atmospheric inflow is 351 kN m, about four times those under uniform and shear inflows. Transverse asymmetry of inflow wind velocity on rotor rotation plane in atmospheric inflow is responsible for the more notable and unstable output of yaw moment. Hence, for the FOWT under atmospheric inflow, the significant yaw moment caused by atmospheric turbulence needs more attention.

The analysis of frequency domain of yaw moment is presented in Fig. 17. In contrast to aerodynamic power and thrust, the peak of natural frequency of pitch f_{pitch} for these wind inflows is not evident, reflecting the limited influence of platform pitch motion on yaw moment. For uniform and shear inflows, the most prominent peak frequency is incident wave frequency f_w, whereas it changes to blade passage frequency f_b in atmospheric scenario. Due to the lateral symmetry of inflow wind, the yaw moment of FOWT in uniform and shear scenarios is dominated by incident wave. This conclusion is changed for atmospheric inflow that the yaw moment of FOWT is dominated by disordered turbulent structures in atmospheric wind field. In high frequency region (i.e., harmonics of blade passage frequency f_b), the PSD of yaw moment under atmospheric inflow is stronger, which is consistent with analysis of aerodynamic performance and suggests that the aerodynamic responses caused by high-frequency small-scale turbulence structures are non-negligible and need more attention.

5.5. Platform motions

The platform motions of FOWT are depicted in Fig. 18 to analyze the impacts of inflow wind conditions on hydrodynamic responses. Note that the incident wave conditions are the same for the three cases, specifically, regular wave with wave height of 3.66m and wave period of 9.7s. Due to the minor discrepancy of aerodynamic responses between uniform inflow and shear inflow, no significant difference of platform motions between the two wind inflows is observed. In addition to a small wave-frequency motion, the platform surge motion also exhibits a remarkable long-drift motion caused by aerodynamic thrust exerted on wind turbine. Among these wind inflows, the platform surge motion exhibits a similar trend, with a minor difference noticeable for atmospheric inflow due to the presence of unstable aerodynamic thrust. The

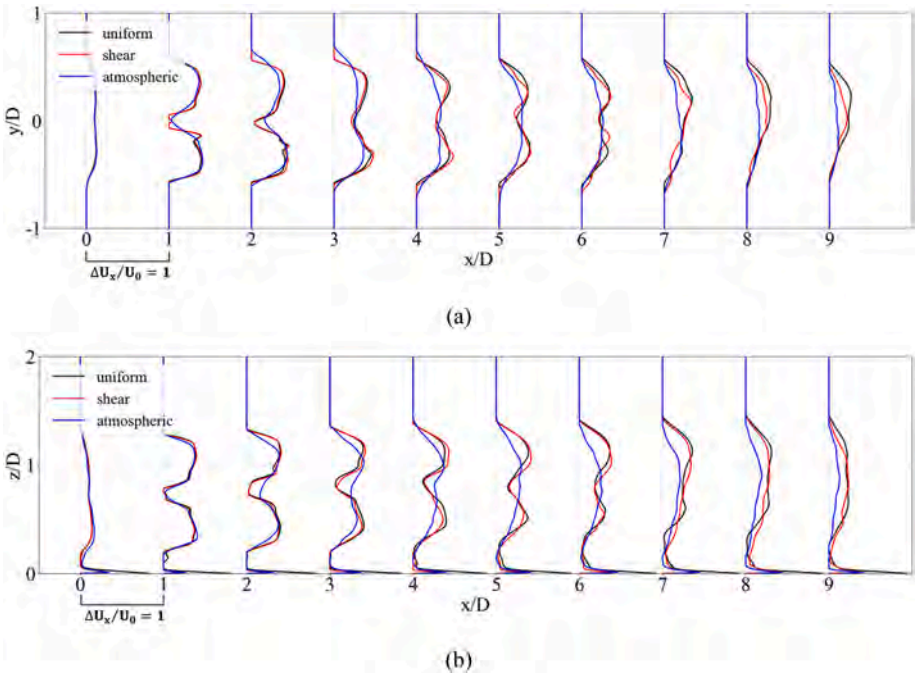

Fig. 21. Velocity deficit of FOWT wake in: (a) hub level plane; (b) vertical plane through rotor center.

hydrodynamic responses of sway and heave for the three wind inflows are small, and thus, their differences for these wind conditions are negligible. Although the varying amplitude of platform roll motion in uniform and shear scenarios is minor, it amplifies to over 3° in atmospheric scenario. Similarly, the variation of platform pitch motion for atmospheric inflow is slightly enhanced compared to that for uniform and shear inflows. The significant difference of hydrodynamic responses for these wind inflows is observed in platform yaw motion. According to the above analysis of yaw moment, its response is significantly intense in atmospheric scenario owing to transverse asymmetry of inflow wind velocity on rotor rotation plane. Consequently, for atmospheric inflow, the amplitude of platform yaw motion exceeds 6°. The atmospheric inflow presents notable effects on rotation of floating platform and may lead to apparent wake deflection, particularly for far wake. This conclusion warrants careful consideration in the development of floating wind farms, particularly considering the significant effects that the wakes of upstream wind turbines have on the operation of downstream wind turbines.

5.6. Wake velocity

Fig. 19 presents the time-averaged (averaged by simulation time of last 10 wave periods) streamwise velocity contours in hub level plane for three inflow wind conditions. To the best of author's knowledge, many studies on the wake of FOWT focus on near-middle wake region of downstream distance 3D-5D due to the expensive computational cost (Arabgolarcheh et al., 2023; Zhou et al., 2022). However, in this work, the wake velocity in far wake region up to downstream distance 9D is visualized to better investigate wake development and evolution. As expected, the significant decreased velocity behind wind turbine is visible. For the uniform inflow, the decreased velocity is clear even at downstream distance 9D, indicating the limited wake recovery. In the shear scenario, the velocity in wind turbine wake exhibits a similar feature compared to the uniform inflow, except that the wake recovery is slightly faster behind downstream distance 6D. The wake velocity under atmospheric inflow is remarkably different compared to above two inflow situations. The faster wake recovery is observed, specifically, the decreased velocity at downstream distance 6D is not obvious, which is beneficial for a downstream wind turbine to increase its power. Besides, the wake is expansive in near wake region, and at downstream distance 4D, wake meandering is visualized.

Fig. 20 depicts the time-averaged streamwise velocity contours in vertical plane through rotor center for three inflow wind conditions. Due to the surge motion of floating platform, the wind turbine rotor is located downstream of initial position $x/D = 0$. The top of spar platform is 10m above the still water level, therefore, there is a small raised low-speed region below wind turbine because of its resistance to flow field. The inclination of wind turbine rotor is clearly observed, resulting from a combination of its 5° tilt and pitch motion of floating platform. Subsequently, this inclination leads to vertical deflection of wake. Although the pitch angles of floating platform among three wind conditions are nearly identical, the vertical deflections of wake under uniform and shear inflows are more pronounced compared to atmospheric inflow. One possible reason is that the impact of vertical component of velocity on wake deflection is suppressed due to the strong interaction between wake of FOWT and ambient atmosphere. In the cases of shear inflow and atmospheric inflow, the wind shear, which involves an increase in wind speed with height, leads to the lower velocity below rotor center in near wake region as compared to the higher velocity above rotor center. The decreased wake velocity in atmospheric scenario is not apparent beyond a downstream distance of 6D. This observation corresponds with the analysis presented in Fig. 19, which indicates a faster wake recovery under atmospheric inflow.

To provide a quantitative insight for wake recovery, the velocity deficits in hub level plane and vertical plane through rotor center are depicted in Fig. 21. It is noteworthy that the freestream velocity varies with height due to the wind shear in shear and atmospheric inflows. In terms of hub level plane, the difference of velocity deficit between uniform inflow and shear inflow is minor until downstream 6D. The velocity deficit in uniform scenario is slightly stronger, indicating that the wind shear can promote wake recovery to some extent. The profiles of the above two wind inflows exhibit bimodal distribution in near wake and unimodal distribution in far wake, and the transitional position is approximately downstream 6D. However, for the atmospheric inflow, this transitional position ahead to downstream 3D. Besides, the interesting observation of wake expansion in near wake is also demonstrated by velocity deficit, in which the width of its profile is wider compared to uniform and shear inflows.

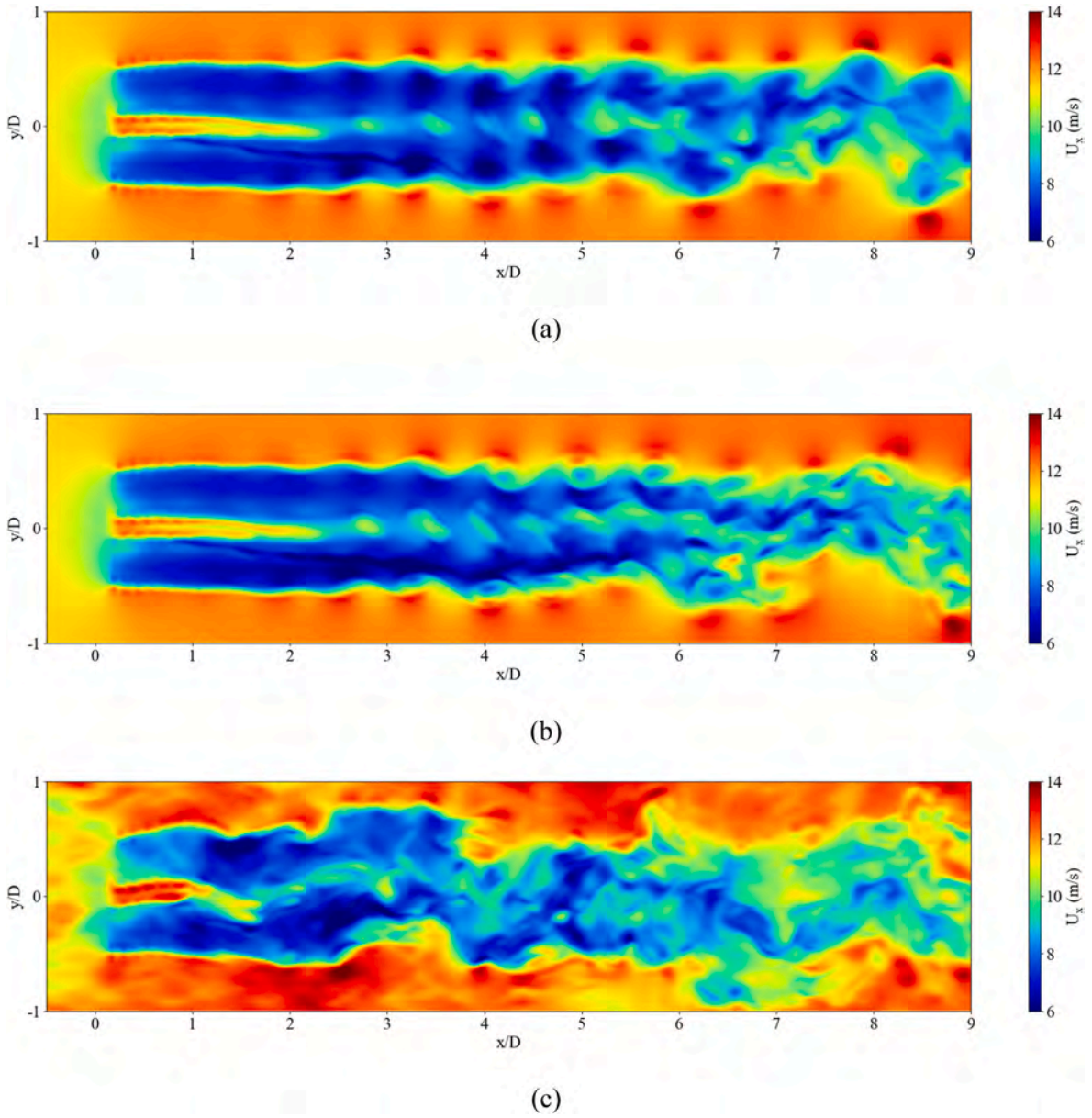

Fig. 22. Instantaneous streamwise velocity contours in hub level plane at time instant of 30th wave periods for different inflow wind conditions: (a) uniform; (b) shear and (c) atmospheric.

The similar conclusions can also be drawn from the velocity deficit in vertical plane through rotor center, as shown in Fig. 21b. For instance, minor difference between uniform inflow and shear inflow, earlier transitional position from bimodal to unimodal and faster wake recovery in atmospheric scenario. Consequently, the power of downstream FOWT will be significantly underestimated if uniform inflow or shear inflow are utilized. The velocity deficit near free surface is pronounced, especially for uniform inflow. This significant velocity deficit is caused by wind-wave interaction, rather than the wind turbine.

Fig. 22 shows the instantaneous streamwise velocity contours in hub level plane for three inflow wind conditions, in which the time instant is 30th wave period (end of simulation time). The wake of FOWT under uniform inflow is stable until the downstream 2D. When the wake further travels downstream, it becomes unstable and slight wake meandering occurs between downstream 2D and 4D. After downstream 4D, the wake breaks and the significant wake meandering is visible. Consequently, external airflow with higher velocity may enters the wake of FOWT, as illustrated at downstream 6.5D and 8D. There is minor difference of the instantaneous wake in hub level plane between shear inflow and uniform inflow. However, the wake of FOWT in atmospheric scenario is more unstable. The wake breakdown and wake meandering appear at downstream 2D, and the wake meandering is more significant in far wake. This observation suggests that the atmospheric inflow has noticeable effect on wake meandering of FOWT.

Similarly, Fig. 23 shows the instantaneous velocity contours in vertical plane through rotor center at the same time instant. The upper wake under uniform inflow remains stable, and no wake breaking is observed during wake evolution. For the lower wake, the broken wake is induced by the high-speed airflow between blade-tip and free surface, and thus, leading to faster velocity recovery in lower far wake. The low-speed air masses in middle wake are obvious, which may be attributed to the reciprocating pitch motion due to wave loads. Those low-speed air masses are also apparent in the wake in shear scenario, but not apparent in atmospheric scenario. The difference of wake between uniform inflow and shear inflow is minor except the high-speed airflow between blade-tip and free surface in uniform scenario. Nonetheless, the wake in

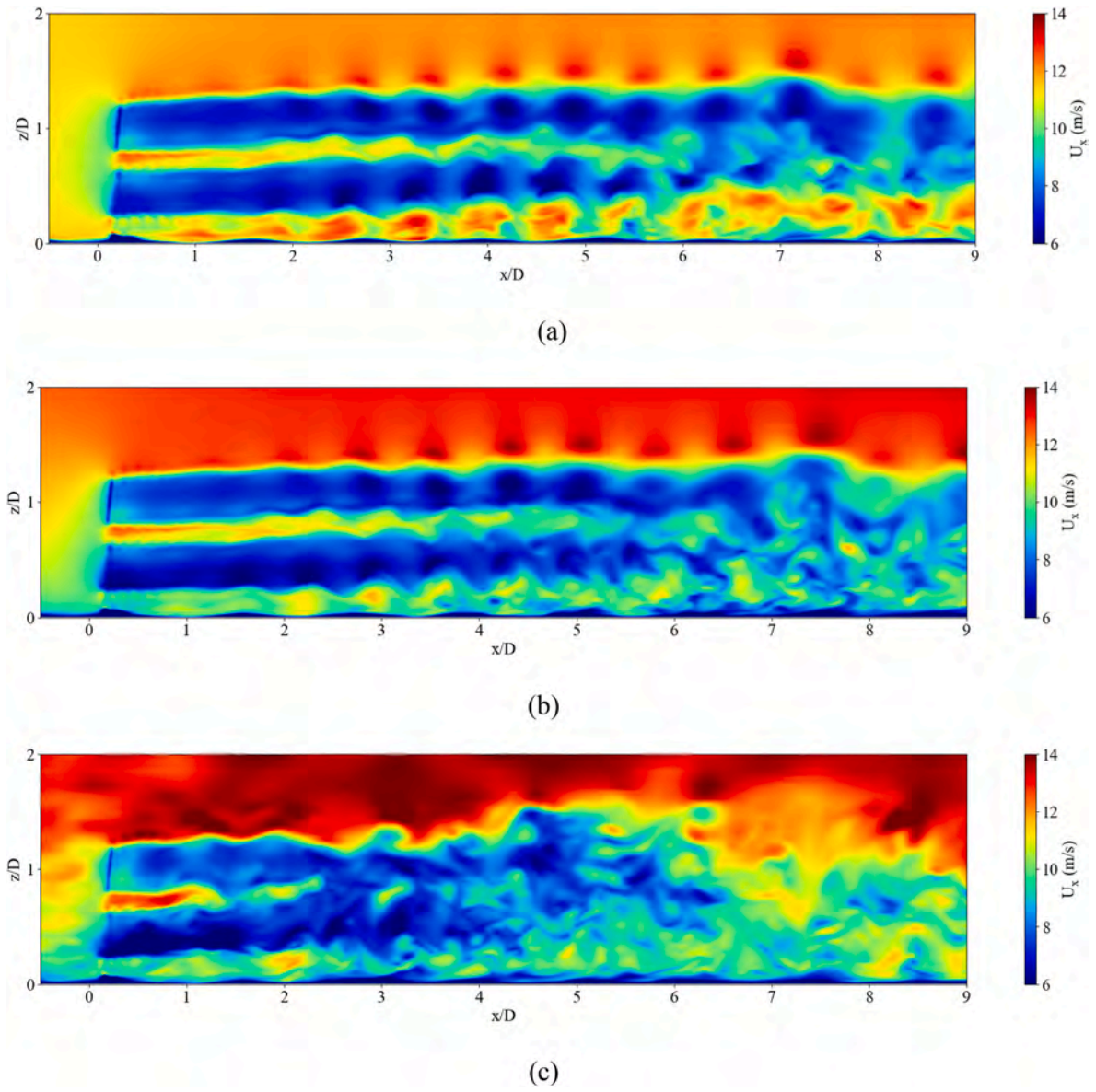

Fig. 23. Instantaneous velocity contours in vertical plane through rotor center at time instant of 30th wave period for different inflow wind conditions: (a) uniform; (b) shear and (c) atmospheric.

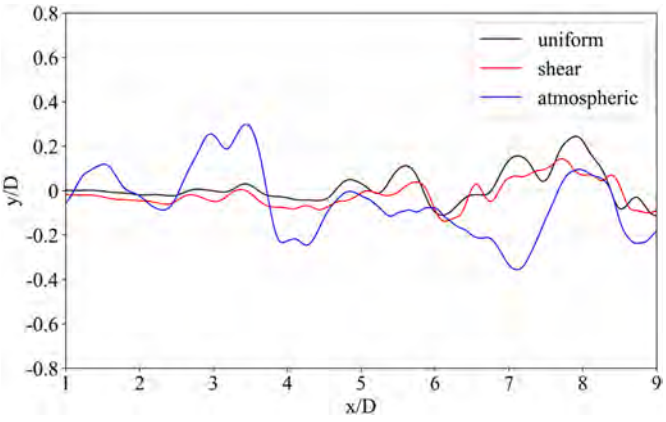

Fig. 24. Lateral wake center in hub level plane at time instant of 30th wave period for different inflow wind conditions.

atmospheric scenario is significantly different. Apart from the earlier wake breaking, more pronounced wake meandering and faster velocity recovery, the wake expansion at downstream 5D is visualized.

5.7. Wake center

Compared with the vertical wake meandering in vertical plane through rotor center, the lateral wake meandering in hub level plane is significant due to the absence of limitation of free surface, even for the uniform inflow and shear inflow. Therefore, the lateral wake center at time instant of 30th wave period is shown in Fig. 24, aiming to provide a quantitative insight on wake meandering. The wake center is determined by applying the Gauss fitting function to velocity deficit profile. It is found that the wake center in uniform scenario remains stable until downstream 5D, then becomes unstable as the wake travels further downstream and the remarkable wake meandering occurs. The wake center in shear scenario exhibits slightly rightward deflection when observed from a downstream perspective. The reason is that the low-speed flow enters the right wake, while the high-speed flow enters the left wake because of the rotation of vortex structures. For the

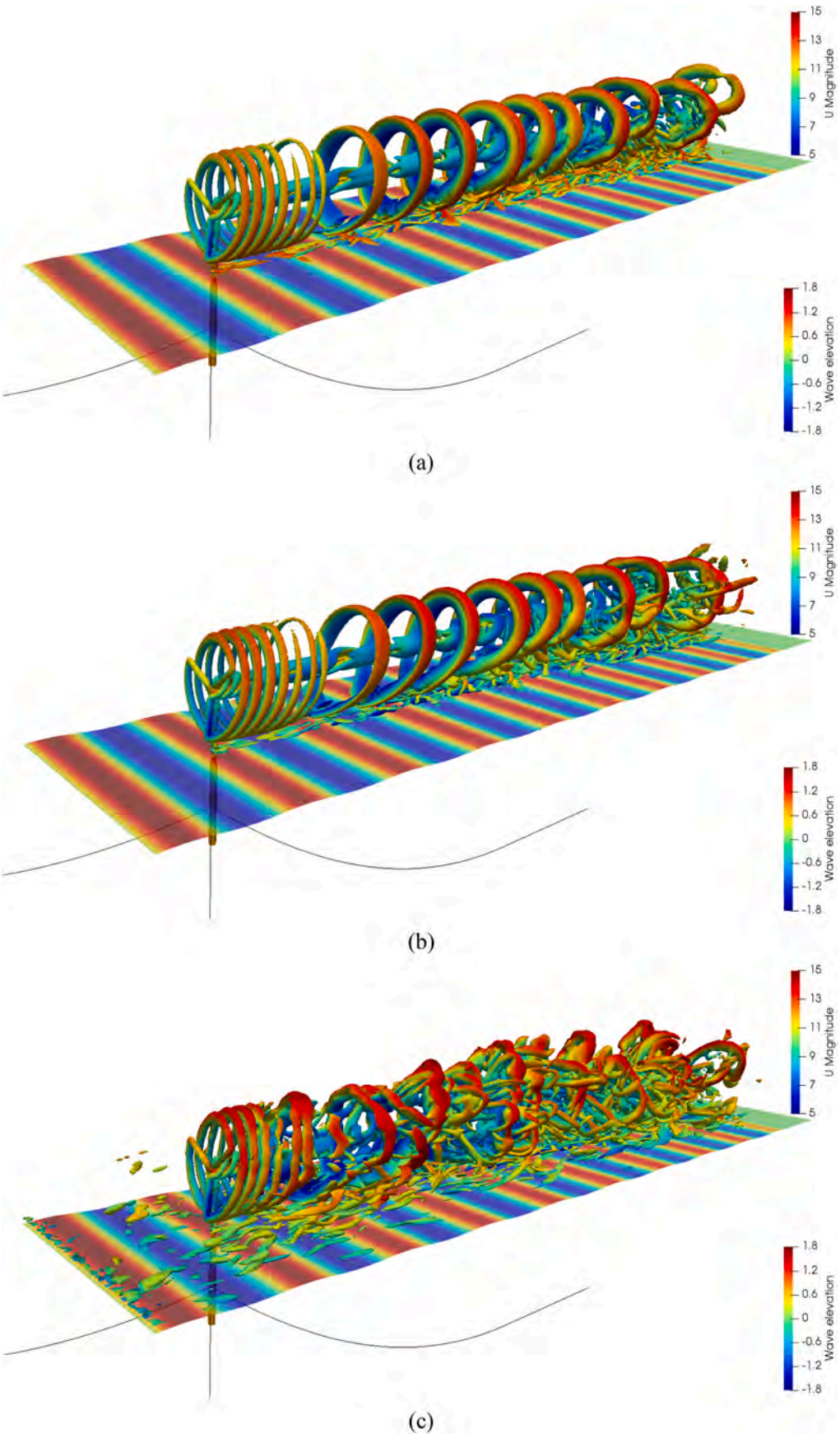

Fig. 25. Vortex structures of FOWT for different inflow wind conditions: (a) uniform; (b) shear and (c) atmospheric.

atmospheric inflow, the wake center is unstable even at downstream 1D. Furthermore, the lateral amplitude of wake meandering is approximately twice that observed in the cases of uniform inflow and shear inflow.

5.8. Vortex structures

Fig. 25 depicts the vortex structures of FOWT for three different wind inflows. The vortex structures are identified by Q-criterion iso-surface (Q = 0.008) and colored by velocity. Observing the case of uniform inflow, the spiral-shaped blade-tip vortices are clear in near wake. Those blade-tip vortices break quickly, generating individual vortex rings. Unlike the blade-tip vortices, the blade-root vortices evolve downstream in a more stable manner and interact with the blade-tip vortices in far wake. The vortices induced by tower are also evident. What's more, the vortex shedding from the top of floating platform shows a strong interaction with the vortex rings. In the far wake, the vortex structures are sophisticated due to the collective interactions among blade-tip vortices, blade-root vortices and platform-induced vortices. In comparison to uniform inflow, the vortex structures under shear inflow exhibit minor distinctions, apart from enhanced shear near free surface. However, the vortex structures in atmospheric scenario show a significant discrepancy compared with both uniform inflow and shear inflow. Due to the atmospheric inflow is turbulent, some vortices upstream the FOWT are apparent. Those vortices strongly interact with wind turbine vortices, and subsequently, resulting in the faster breakdown of blade-tip vortices. In the further wake, there is an absence of vortex rings, as typically seen in cases of uniform inflow and shear inflow. Instead, the wake presents the large-scale fragmented vortices. In the far wake, more complex and smaller vortices become apparent. A conclusion can be drawn that the atmospheric inflow imparts a heightened level of complexity to the vortex structures of FOWT. This observation needs to be carefully considered and treated when assessing the wake effects between multiple FOWTs.

6. Conclusions

In this study, we numerically investigate the effects of atmospheric turbulence inflow on aero-hydrodynamics and wake characteristics of FOWT. The numerical simulations are performed using our well-validated in-house solver, FOWT-UALM-SJTU. To generate the realistic atmospheric inflow, the LES with long-duration simulation is employed.

Compared to uniform inflow and shear inflow, the power of FOWT under atmospheric inflow is more unstable. The PSD of power exhibits higher intensity in high frequency region due to high-frequency small-scale turbulence structures in atmospheric inflow. A similar observation holds for the analysis of thrust. The variation of yaw moment in atmospheric scenario is significantly drastic. Consequently, the dominant frequency of PSD of yaw moment is blade passage frequency f_b, rather than the incident wave frequency f_w observed in uniform and shear scenarios, indicating that the yaw moment is dominated by disordered turbulent structures. The significant variation of yaw moment in atmospheric scenario leads to the remarkable response of platform yaw motion, with its amplitude exceeding 6°.

The wake recovery in atmospheric scenario is faster. Specifically, the transition from bimodal distribution to unimodal distribution in velocity deficit profile occurs at downstream 3D, whereas in the uniform and shear inflow scenarios, this transition occurs at approximately downstream 6D. The wake breakdown and significant wake meandering in atmospheric scenario occurs earlier, with even more significant wake meandering observed in far wake. This observation is further confirmed through quantitative analysis of wake center. The vortices in freestream atmospheric inflow interact with wind turbine vortices, resulting in the accelerated breakdown of blade-tip vortices. In the far wake, the absence of vortex rings in atmospheric scenario is observed, along with the presence of more complex and smaller vortices.

Our results show the significant effects of atmospheric inflow on wake characteristics of FOWT. To provide valuable insights into floating wind farms, it is imperative and meaningful to explore the operation performance of downstream FOWTs in wakes of upstream FOWTs subjected to atmospheric inflow. Various configurations, such as tandem and offset layouts, are recommended. Furthermore, it is advisable to conduct studies that examine the influence of different thermal stabilities on the wake characteristics of FOWTs.

CRediT authorship contribution statement

Shun Xu: Writing – original draft, Visualization, Validation, Software, Methodology, Investigation, Data curation, Conceptualization. **Xiaolong Yang:** Writing – review & editing, Validation, Resources. **Weiwen Zhao:** Visualization, Validation, Methodology, Investigation. **Decheng Wan:** Writing – review & editing, Supervision, Methodology, Investigation, Funding acquisition, Data curation, Conceptualization.

Declaration of competing interest

The authors declare that they have no known competing financial interests or personal relationships that could have appeared to influence the work reported in this paper.

Data availability

Data will be made available on request.

Acknowledgement

This work is supported by the National Natural Science Foundation of China (52131102), to which the authors are most grateful.

References

Abkar, M., Porté-Agel, F., 2015. Influence of atmospheric stability on wind-turbine wakes: a large-eddy simulation study. Phys. Fluids 27 (3), 035104.
Arabgolarcheh, A., Rouhollahi, A., Benini, E., 2023. Analysis of middle-to-far wake behind floating offshore wind turbines in the presence of multiple platform motions. Renew. Energy 208, 546–560.
Cao, H., Wan, D., 2014. Development of multidirectional nonlinear numerical wave tank by naoe-FOAM-SJTU solver. Int.J. Ocean Syst. Eng. 4 (1), 49–56.
Cao, H., Wang, X., Liu, Y., et al., 2013. Numerical prediction of wave loading on a floating platform coupled with a mooring system. In: Proceedings of the the Twenty-Third International Offshore and Polar Engineering Conference. OnePetro. F.
Chanprasert, W., Sharma, R.N., Cater, J.E., et al., 2022. Large Eddy Simulation of wind turbine fatigue loading and yaw dynamics induced by wake turbulence. Renew. Energy 190, 208–222.
Chen, P., Chen, J., Hu, Z., 2020. Review of experimental-numerical methodologies and challenges for floating offshore wind turbines. J. Mar. Sci. Appl. 19 (3), 339–361.
Chen, Z., Wang, X., Guo, Y., et al., 2021. Numerical analysis of unsteady aerodynamic performance of floating offshore wind turbine under platform surge and pitch motions. Renew. Energy 163, 1849–1870.
Chen, S., Zhao, W., Wan, D., 2022. Turbulent structures and characteristics of flows past a vertical surface-piercing finite circular cylinder. Phys. Fluids 34 (1), 015115.
Cheng, P., Huang, Y., Wan, D., 2019. A numerical model for fully coupled aero-hydrodynamic analysis of floating offshore wind turbine. Ocean Eng. 173, 183–196.
Churchfield, M.J., Lee, S., Michalakes, J., et al., 2012. A numerical study of the effects of atmospheric and wake turbulence on wind turbine dynamics. J. Turbul. 13, N14.
Dong, J., Viré, A., 2022. The aerodynamics of floating offshore wind turbines in different working states during surge motion. Renew. Energy 195, 1125–1136.
Feng, X., Fang, J., Lin, Y., et al., 2023. Coupled aero-hydro-mooring dynamic analysis of floating offshore wind turbine under blade pitch motion. Phys. Fluids 35 (4), 045131.
Fleming, P.A., Gebraad, P.M., Lee, S., et al., 2014. Evaluating techniques for redirecting turbine wakes using SOWFA. Renew. Energy 70, 211–218.
Fu, S., Li, Z., Zhu, W., et al., 2023. Study on aerodynamic performance and wake characteristics of a floating offshore wind turbine under pitch motion. Renew. Energy 205, 317–325.
Hansen, K.S., Barthelmie, R.J., Jensen, L.E., et al., 2012. The impact of turbulence intensity and atmospheric stability on power deficits due to wind turbine wakes at Horns Rev wind farm. Wind Energy 15 (1), 183–196.

Huang, Y., Wan, D., 2019. Investigation of interference effects between wind turbine and spar-type floating platform under combined wind-wave excitation. Sustainability 12 (1), 246.
Huang, Y., Cheng, P., Wan, D., 2019. Numerical analysis of a floating offshore wind turbine by coupled aero-hydrodynamic simulation. J. Mar. Sci. Appl. 18 (1), 82–92.
Huang, H., Liu, Q., Yue, M., et al., 2023a. Fully coupled aero-hydrodynamic analysis of a biomimetic fractal semi-submersible floating offshore wind turbine under wind-wave excitation conditions. Renew. Energy 203, 280–300.
Huang, Y., Zhao, W., Wan, D., 2023b. Wake interaction between two spar-type floating offshore wind turbines under different layouts. Phys. Fluids 35 (9), 097102.
Johlas, H., Martinez, L., Schmidt, D., et al., 2019. Large Eddy Simulations of Floating Offshore Wind Turbine Wakes with Coupled Platform Motion. National Renewable Energy Lab. (NREL), Golden, CO (United States).
Johlas, H.M., Martínez-Tossas, L.A., Lackner, M.A., et al., 2020. Large eddy simulations of offshore wind turbine wakes for two floating platform types. J. Phys.: Conf. Ser. IOP Publ. 1452 (1), 012034.
Jonkman, J., 2010. Definition of the Floating System for Phase IV of OC3. National Renewable Energy Lab. (NREL), Golden, CO (United States).
Jonkman, J., Musial, W., 2010. Offshore Code Comparison Collaboration (OC3) for IEA Wind Task 23 Offshore Wind Technology and Deployment. National Renewable Energy Lab. (NREL), Golden, CO (United States).
Jonkman, J., Butterfield, S., Musial, W., et al., 2009. Definition of a 5-MW Reference Wind Turbine for Offshore System Development. National Renewable Energy Lab. (NREL), Golden, CO (United States).
Kleine, V.G., Franceschini, L., Carmo, B.S., et al., 2022. The stability of wakes of floating wind turbines. Phys. Fluids 34 (7), 074106.
Lee, H., Lee, D.J., 2019. Effects of platform motions on aerodynamic performance and unsteady wake evolution of a floating offshore wind turbine. Renew. Energy 143, 9–23.
Li, L., Liu, Y., Yuan, Z., et al., 2018. Wind field effect on the power generation and aerodynamic performance of offshore floating wind turbines. Energy 157, 379–390.
Li, Z., Liu, X., Yang, X., 2022. Review of turbine parameterization models for large-eddy simulation of wind turbine wakes. Energies 15 (18), 6533.
Lu, H., Porté-Agel, F., 2011. Large-eddy simulation of a very large wind farm in a stable atmospheric boundary layer. Phys. Fluids 23 (6), 065101.
Mancini, S., Boorsma, K., Caboni, M., et al., 2020. Characterization of the unsteady aerodynamic response of a floating offshore wind turbine to surge motion. Wind Energy Sci. 5 (4), 1713–1730.
Ning, X., Wan, D., 2019. LES Study of wake meandering in different atmospheric stabilities and its effects on wind turbine aerodynamics. Sustainability 11 (24), 6939.
Otter, A., Murphy, J., Pakrashi, V., et al., 2022. A review of modelling techniques for floating offshore wind turbines. Wind Energy 25 (5), 831–857.
Porté-Agel, F., Bastankhah, M., Shamsoddin, S., 2020. Wind-turbine and wind-farm flows: a review. Boundary-Layer Meteorol. 174 (1), 1–59.
Schumann, U., 1975. Subgrid scale model for finite difference simulations of turbulent flows in plane channels and annuli. J. Comput. Phys. 18 (4), 376–404.
Shen, Z., Cao, H., Ye, H., et al., 2012a. Manual of CFD Solver for Ship and Ocean Engineering Flows: Naoe-FOAM-SJTU. Shanghai Jiao Tong University, Shanghai, China.
Shen, Z., Ye, H., Wan, D., 2012b. Motion response and added resistance of ship in head waves based on RANS simulations. Chin. J. Hydrodynam. 27 (6), 621–633.
Spalart, P.R., Deck, S., Shur, M.L., et al., 2006. A new version of detached-eddy simulation, resistant to ambiguous grid densities. Theor. Comput. Fluid Dynam. 20, 181–195.
Tran, T.T., Kim, D.H., 2016. Fully coupled aero-hydrodynamic analysis of a semi-submersible FOWT using a dynamic fluid body interaction approach. Renew. Energy 92, 244–261.
Troldborg, N., Sørensen, J.N., Mikkelsen, R., 2007. Actuator line simulation of wake of wind turbine operating in turbulent inflow. J. Phys.: Conf. Ser. IOP Publ. 75 (1), 012063.
Wang, J., Zhao, W., Wan, D., 2019. Development of naoe-FOAM-SJTU solver based on OpenFOAM for marine hydrodynamics. J. Hydrodyn. 31, 1–20.
Wang, T., Cai, C., Wang, X., et al., 2023. Evolution mechanism of wind turbine wake structure in yawed condition by actuator line method and theoretical analysis. Energy Convers. Manag. 281, 116852.
Xu, S., Xue, Y., Zhao, W., et al., 2022. A review of high-fidelity computational fluid dynamics for floating offshore wind turbines. J. Mar. Sci. Eng. 10 (10), 1357.
Xu, S., Zhuang, T., Zhao, W., et al., 2023a. Numerical investigation of aerodynamic responses and wake characteristics of a floating offshore wind turbine under atmospheric boundary layer inflows. Ocean Eng. 279, 114527.
Xu, S., Wang, N., Zhuang, T., et al., 2023b. Large eddy simulations of wake flows around a floating offshore wind turbine under complex atmospheric inflows. Int. J. Offshore Polar Eng. 33 (1), 1–9.
Yang, H., Ge, M., Gu, B., et al., 2022. The effect of swell on marine atmospheric boundary layer and the operation of an offshore wind turbine. Energy 244, 123200.
Zhang, Y., Kim, B., 2018. A fully coupled computational fluid dynamics method for analysis of semi-submersible floating offshore wind turbines under wind-wave excitation conditions based on OC5 data. Appl. Sci. 8 (11), 2314.
Zhao, W., Wan, D., 2015. Numerical study of interactions between phase II of OC4 wind turbine and its semi-submersible floating support system. J. Ocean Wind Energy 2 (1), 45–53.
Zhou, Y., Xiao, Q., Liu, Y., et al., 2022. Exploring inflow wind condition on floating offshore wind turbine aerodynamic characterisation and platform motion prediction using blade resolved CFD simulation. Renew. Energy 182, 1060–1079.